The Pulsating Helium-atmosphere White Dwarfs. I. New DBVs from the Sloan Digital Sky Survey

Zachary P. Vanderbosch[1] , J. J. Hermes[2] , Don E. Winget[3,4] , Michael H. Montgomery[3,4] , Keaton J. Bell[5,8] ,
Atsuko Nitta[6], and S. O. Kepler[7]

[1] Division of Physics, Mathematics, and Astronomy, California Institute of Technology, Pasadena, CA 91125, USA; zvanderb@caltech.edu
[2] Department of Astronomy, Boston University, Boston, MA-02215, USA
[3] Department of Astronomy, University of Texas at Austin, Austin, TX-78712, USA
[4] McDonald Observatory, Fort Davis, TX-79734, USA
[5] DIRAC Institute, Department of Astronomy, University of Washington, Seattle, WA-98195, USA
[6] Gemini Observatory, 670 North A'ohoku Place, Hilo, HI 96720, USA
[7] Instituto de Física, Universidade Federal do Rio Grande do Sul, 91501-900 Porto-Alegre, RS, Brazil

Abstract

We present a dedicated search for new pulsating helium-atmosphere (DBV) white dwarfs from the Sloan Digital Sky Survey using the McDonald 2.1 m Otto Struve Telescope. In total we observed 55 DB and DBA white dwarfs with spectroscopic temperatures between 19,000 and 35,000 K. We find 19 new DBVs and place upper limits on variability for the remaining 36 objects. In combination with previously known DBVs, we use these objects to provide an update to the empirical extent of the DB instability strip. With our sample of new DBVs, the red edge is better constrained, as we nearly double the number of DBVs known between 20,000 and 24,000 K. We do not find any new DBVs hotter than PG 0112+104, the current hottest DBV is at $T_{\rm eff} \approx$ 31,000 K, but do find pulsations in four DBVs with temperatures between 27,000 and 30,000 K, improving empirical constraints on the poorly defined blue edge. We investigate the ensemble pulsation properties of all currently known DBVs, finding that the weighted mean period and total pulsation power exhibit trends with effective temperature that are qualitatively similar to the pulsating hydrogen-atmosphere white dwarfs.

1. Introduction

White dwarf stars are the endpoint of stellar evolution for the vast majority of stars in our galaxy. About 20% of white dwarfs have optical spectra dominated by He lines, the DB and DBA stars (Kleinman et al. 2013; Kepler et al. 2019). DBs show only He I lines, while DBAs also show evidence for a trace of atmospheric H via Hα or Hβ absorption. As these white dwarfs cool monotonically throughout their lifetimes, they eventually reach the DB instability strip that covers effective temperatures, $T_{\rm eff}$, between 30,000 and 22,000 K at gravities of $\log(g\ [\mathrm{cm\ s^{-2}]}) =$ 8.0. Here, a He partial ionization region forms near the surface, and interior pulsations are driven to observable amplitudes. The exact location of the instability strip is mass dependent, with higher-mass white dwarfs pulsating at higher temperatures. For the more common DA white dwarfs, those with H-dominated atmospheres, the instability strip occurs at lower temperatures (12,500 > $T_{\rm eff}$ > 10,500 K at $\log(g) = 8.0$).

Following the detections of pulsations in DA white dwarfs (Landolt 1968), pulsations in DBs were first predicted and then discovered by Winget et al. (1982) in GD 358, the prototypical DBV. Since then, DBVs have remained difficult to find relative to their DAV counterparts due to faster cooling rates and the relative rarity of white dwarfs with He-dominated versus

H-dominated atmospheres. Only 28 DBVs are currently known (see Córsico et al. 2019; Duan et al. 2021). The largest boost in DBV numbers came from Nitta et al. (2009), who followed up candidates from the Sloan Digital Sky Survey (SDSS) using time-series photometry from McDonald Observatory. Nitta et al. doubled the number from 9 to 18, but most DBVs have been found just one or two at a time. Four pulsators have been identified as DBAVs so far due to detections of trace H (Giammichele et al. 2018; Rolland et al. 2018).

Increasing the number of known DBVs is beneficial for several reasons. More DBVs provide more candidates for which asteroseismic modeling can be used to probe the interior composition and structure of DBs (e.g., Timmes et al. 2018; Charpinet et al. 2019). These models place valuable boundary conditions on stellar evolution, particularly for DBs whose evolutionary origins are still debated. Below 30,000−40,000 K, some DBs likely appear due to the convective dilution of a thin, primordial H-layer ($M_{\rm H} = 10^{-16}$–$10^{-14}\ M_\odot$) within the more massive He convection zone (MacDonald & Vennes 1991; Rolland et al. 2018), but this model cannot currently explain all DBs, especially those with high H contents whose H-layer ought to have survived convective dilution and remained as DAs. Other evolutionary channels, such as binary mergers (Nather et al. 1981), may account for some DBs, which would produce different internal structures that can be probed by asteroseismic models. To date, only a handful of DBVs have enough detected periods for asteroseismic modeling to be performed, such as GD 358 (Bischoff-Kim et al. 2019), CBS 114 (Metcalfe et al. 2005), PG 0112+104 (Hermes et al. 2017a), KIC 8626021 (Bischoff-Kim et al. 2014; Giammichele et al. 2018),

TIC 257459955 (Bell et al. 2019), and EPIC 228782059 (Duan et al. 2021).

Finding more DBVs also increases the chance of finding candidates for stable pulsations. Long-term secular changes in pulsation periods can be used to measure white dwarf cooling rates (e.g., Kepler et al. 2021), while periodic variations in pulsation arrival times can be used to search for planetary companions (Winget et al. 2003; Mullally et al. 2008). Plasmon neutrino emission is thought to be the dominant source of energy loss in white dwarfs above 25,000 K (Winget et al. 2004), which means that hot DBVs probe a unique parameter space that is not accessible to stable DAV pulsators. Fortunately, blue-edge (hot) pulsating white dwarfs are expected to have more stable pulsations relative to red-edge (cool) pulsators because the propagation cavities of their excited modes do not yet interact with the base of the convection zone (Montgomery et al. 2020). From a theoretical perspective, stable DBVs are therefore more likely to be found near the blue edge and probe relatively high neutrino emission rates.

To date, only one DBV has been identified as a good candidate for stable pulsations and used to place preliminary constraints on its cooling rate (PG 1351+456; Redaelli et al. 2011; Battich et al. 2016), although it is likely too cool for neutrino emission to be the dominant source of energy loss. Of the two hottest DBVs, only PG 0112+104 remains a good candidate for stable pulsations as EC 20058−5234 has shown long-term period changes that cannot be accounted for by white dwarf cooling processes (Dalessio et al. 2013; Sullivan 2017). Unfortunately, even though PG 0112+104 does exhibit a high degree of stability throughout its ≈80-day K2 campaign with the Kepler spacecraft, the modes are very low amplitude (<0.03% in the Kepler bandpass) and therefore difficult to detect and monitor with ground-based observations. Finding a hot DBV with stable pulsations that is both bright and has a relatively high amplitude would provide a unique opportunity to test white dwarf cooling theory.

Another use in finding more DBVs is placing empirical constraints on the extent of the DB instability strip. The location of the hot (blue) edge is strongly dependent on the convective efficiency at the base of the convection zone (Fontaine & Brassard 2008; Córsico et al. 2009; Van Grootel et al. 2017), and theory suggests it might be used to calibrate the ratio of mixing length to pressure scale height (α) used in 1D mixing-length theory (e.g., Beauchamp et al. 1999). The assumed convective efficiency has strong implications for the diffusion timescales of heavy metals accreted from disrupted planetary material, which are needed to accurately infer bulk planetary compositions (e.g., Zuckerman et al. 2007; Dufour et al. 2010a; Melis et al. 2011; Farihi et al. 2013, 2016; Bauer & Bildsten 2019; Xu et al. 2019; Hoskin et al. 2020). The cool (red) edge has traditionally defied a self-consistent theoretical description, but was most recently calculated by Van Grootel et al. (2017) using an energy leakage criterion and found to be at 22,000 K at $\log(g) = 8.0$, about 1000 K cooler than the observed red edge.

Two main factors currently limit the ability to properly define the observed blue and red edges: (1) the small number of both hot and cool DBVs, and (2) the difficulty of obtaining accurate effective temperatures. The observed blue edge is currently defined by one object, PG 0112+104 (Shipman et al. 2002; Provencal et al. 2003; Hermes et al. 2017a), with $T_{\rm eff} = 31,000$ K and $\log(g) = 7.8$ (Dufour et al. 2010b;

Rolland et al. 2018). PG 0112+104 is about 2000 K hotter than the theoretical blue edge proposed by Van Grootel et al. (2017), suggesting that a higher convective efficiency (higher α) is required to explain the observed blue edge. Pulsations in PG 0112+104 have extremely low amplitudes, with maximum amplitudes detected by Kepler observations of about 0.03% (Hermes et al. 2017a). This suggests that many DBs that have historically been considered non-pulsators beyond the blue edge might indeed pulsate with amplitudes that are difficult to detect without extensive observations (e.g., Castanheira et al. 2010).

The atmospheric parameters for DBs ($T_{\rm eff}$, $\log(g)$, and H/He) are typically determined via a comparison of observed and model spectra (the spectroscopic technique; Eisenstein et al. 2006a; Bergeron et al. 2011) or broadband photometry (the photometric technique; Bergeron et al. 1997; Genest-Beaulieu & Bergeron 2019a). Depending on which method and which set of atmospheric models are used to obtain atmospheric parameters, the observed red edge can vary in location between 20,000 and 23,000 K and is often defined by fewer than five objects. Similar effects on the DA instability strip have also been observed when comparing spectroscopic and photometric atmospheric parameters, with photometric parameters derived from Pan-STARRS1 grizy photometry being a few hundred degrees cooler on average within the DA instability strip than the spectroscopic technique (Bergeron et al. 2019; Vincent et al. 2020). When defining the blue and red edges observationally, it is also important to find nonvariable DBs near to or within the instability strip. Nitta et al. (2009) reported several DBs that were not observed to vary (NOV), but most had only one night of observations and variability limits above 0.5%, leaving their NOV status uncertain. Many DBVs exhibit pulsation amplitudes below this limit, and destructive beating in multiperiodic pulsators can often make them appear nonvariable in short single-night runs.

Even with more DBVs, however, the large uncertainties in their effective temperatures pose a significant challenge in defining the DB instability strip. DBV temperatures often vary by large amounts between studies due in large part to the insensitivity of He I absorption lines to changes in $T_{\rm eff}$ throughout the instability strip (see Figure 2 of Bergeron et al. 2011). The peak He I line strength occurs around 25,000 K, which often leads to degenerate hot and cold solutions for DBVs, especially those with low signal-to-noise (S/N) observations. A common practice today is to use broadband photometry, such as the SDSS ugriz (e.g., Koester & Kepler 2015; Kepler et al. 2019), to try and break the degeneracy with a photometric fit, but this does not always guarantee the correct solution. Masses for DBs have also been found to be unreliable, although only at lower temperatures ($T_{\rm eff} \lesssim 16,000$ K), which is suspected to arise from an improper treatment of neutral broadening (see Koester & Kepler 2015; Cukanovaite et al. 2018).

An additional source of temperature uncertainty comes from the presence of trace undetected H. This effect was first studied by Beauchamp et al. (1999), who found that atmospheric parameters for DBVs determined assuming pure-He atmospheres were in some cases 3000 K hotter than those with [H/He] = $\log(N_{\rm H}/N_{\rm He}) = -3$. Subsequent studies that placed better observational constraints on [H/He] using spectroscopic Hα coverage (Voss et al. 2007; Bergeron et al. 2011; Rolland et al. 2018) found this systematic effect to be much smaller on average, on the order of a few hundred Kelvin. Regardless, in cases where only upper limits on

[H/He] can be determined, a systematic uncertainty in T_{eff} is present. It is also uncertain whether trace H should affect the location of the instability strip for DBAs. Some authors suggest that the DBA instability should be a few hundred degrees cooler (Fontaine & Brassard 2008), and Bergeron et al. (2011) find that the three DBAVs in their sample pulsate at lower T_{eff} than the DBVs, but Van Grootel et al. (2017) found that trace H has no effect on the theoretical blue or red edges.

To address many of the issues mentioned above and use DBVs to their fullest potential, finding more DBVs (and NOVs) is the first step. The SDSS is a photometric and spectroscopic survey (York et al. 2000; Eisenstein et al. 2011; Blanton et al. 2017) covering more than 10,000 deg² of the northern sky. To date, it is still the gold standard in terms of spectroscopic surveys, having increased the number of spectroscopically confirmed white dwarfs since the McCook & Sion (1999) catalog by more than an order of magnitude, from ∼ 3000 to more than 30,000 (Kleinman et al. 2004; Eisenstein et al. 2006b; Kleinman et al. 2013; Kepler et al. 2015, 2016, 2019). Newer catalogs based on Gaia photometry have increased the number of white dwarfs by yet another order of magnitude (Gentile Fusillo et al. 2019, 2021), but without spectroscopic identifications, it is difficult to efficiently identify good DB candidates near the instability strip. Therefore, the SDSS is still one of the best resources available for increasing the number of known DBVs, allowing for more reliable identification of candidates for follow-up time-series photometry.

In this work, we report an effort to identify DBVs using time-series photometry from McDonald Observatory. Similar to Nitta et al. (2009), we identify candidate pulsating DBs and DBAs using atmospheric parameters determined from the SDSS DR10, DR12, and DR14 catalogs (Koester & Kepler 2015; Kepler et al. 2019). In Section 2 we discuss our target selection process and accompanying McDonald time-series observations, in Section 3 we report on the new DBVs we discovered, their detected periods, and the variability limits we place on NOVs, in Section 4 we discuss the updated DB instability strip, in Section 5 we discuss the ensemble pulsation properties of the DBVs, and in Section 6 we provide concluding remarks.

2. Observations

2.1. Target Selection

We selected our targets using the catalog of spectroscopically confirmed DB white dwarfs identified in SDSS data releases 10 and 12 (Koester & Kepler 2015, hereafter KK15) and data release 14 (Kepler et al. 2019). In an effort to better define the edges of the instability strip, and because DB spectroscopic temperatures are often highly uncertain, we extended our search a few thousand degrees hotter and cooler with respect to both the empirical temperature range for DBVs and to the theoretical blue and red edges of Van Grootel et al. (2017). Ultimately, our search covered DB white dwarfs with spectroscopic effective temperatures between roughly 19,000 and 35,000 K, including some DBAs. In Figure 1 we show the effective temperatures and surface gravities of our sample of observed objects, 55 in total, compared to the sample of previously identified DBVs and the DBs from KK15.

Based on previous efforts to discover new DBVs in the SDSS (e.g., Nitta et al. 2009), we expected a large fraction of our targets to result in null detections of pulsations, i.e., NOV. For instance, just ≈30% of the DB white dwarfs observed by Nitta et al. (2009) were found to pulsate. This low detection
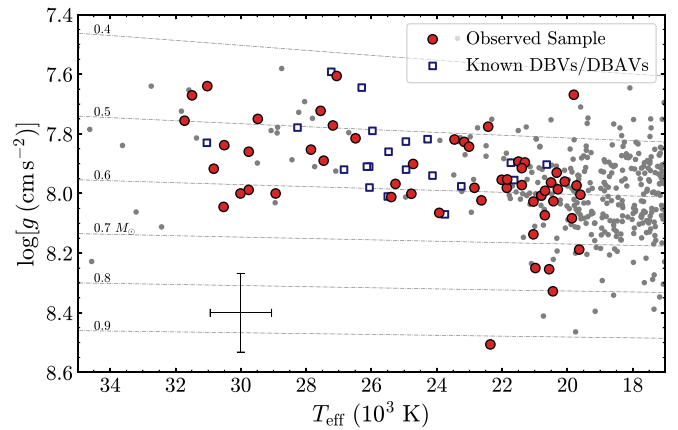

Figure 1. The sample of 55 DB/DBAs observed in this work (red circles) compared to the full sample of DB/DBA white dwarfs from Koester & Kepler (2015; gray circles) in the $\log(g)$ vs. T_{eff} plane. Previously identified DBVs are marked with open blue squares, while dash–dotted gray lines show evolutionary tracks for white dwarfs of various masses with thin hydrogen envelopes ($M_H/M_\star = 10^{-10}$; Bédard et al. 2020). A typical error bar size for objects between 22,000 and 30,000 K is shown in the bottom left corner.

rate is partly influenced by unreliable temperature determinations, such that objects whose temperatures place them within the instability may in fact lie outside the instability strip.

Still, the null detections of pulsations for objects near the blue or red edge place useful constraints on the boundaries of the DB instability strip, so we aimed to place limits on the variability of <5 mma (0.5%) for all objects. We also aimed to observe all objects on two separate nights to minimize the chance that we observed a pulsating DB during a phase where destructive beating between two or more pulsation modes reduced the photometric variability below our detection threshold. We were able to obtain two nights of photometry for 48 out of 55 objects in our sample. Last, we mostly observed DB white dwarfs with g-band magnitudes ≲19 so we could place stronger NOV limits on null detections. The average SDSS g-band magnitude of our sample is about 17.9, with the full sample covering 15.7 to 19.3 mag. Only 3 out of 55 objects had magnitudes fainter than $g = 19$.

2.2. McDonald Photometry

We carried out time-series photometry on all of our targets using a Princeton Instruments ProEM frame-transfer CCD attached to the McDonald Observatory 2.1 m Otto Struve Telescope. We observed exclusively with a blue-bandpass BG40 filter that covers wavelengths between 3500 and 6500 Å. Exposure times range from 3 to 30 s depending on object brightness and weather conditions, with individual runs averaging 2.4 hr in length. A full summary of our observations can be found in Table 1.

Using standard calibration frames taken during each night of observations, we dark- and flat-field corrected our images using the IRAF reduction suite. We then performed circular aperture photometry using the IRAF ccd_hsp package (Kanaan et al. 2002), with aperture radii ranging from 2 to 10 pixels in half-pixel steps. Local sky subtraction was performed for each object using an annulus centered on each aperture.

We generated divided light curves using the WQED reduction software (Thompson & Mullally 2013), selecting the aperture size that maximized the S/N of the light curve. We removed any long-term trends from the divided light curve with

Table 1
Summary of McDonald 2.1 m Observations

Name (SDSS J)	Date	ΔT (hr)	t_{exp} (s)	Name (SDSS J)	Date	ΔT (hr)	t_{exp} (s)	Name (SDSS J)	Date	ΔT (hr)	t_{exp} (s)
002458.42+245834.2	2017 Jul 28	2.13	10	082316.32+233317.8	2017 Dec 12	1.68	10		2018 May 16	2.82	5
	2017 Jul 30	1.69	10		2017 Dec 16	1.79	20	154201.50+502532.1	2018 May 12	1.15	5
	2017 Oct 21	4.16	20	083035.14+564459.4[a]	2017 Dec 12	1.31	15		2018 May 13	2.92	5
011607.92+330154.3[a]	2017 Dec 12	1.80	15		2018 Jan 23	1.07	15	155327.56+150545.7[a]	2018 May 13	2.86	15
	2017 Dec 13	1.86	15	083415.45+254819.9[a]	2018 Mar 14	1.11	15	155921.08+190407.8	2017 May 19	2.84	10
012752.18+140622.9[a]	2018 Sep 10	3.45	10		2018 Mar 16	3.11	15		2017 May 21	0.77	5
	2017 Sep 11	3.92	10	084211.30+461819.0[a]	2017 Dec 14	2.76	15		2017 May 22	2.22	15
014945.65+223016.4	2018 Sep 12	1.79	15	084350.85+361419.5	2017 Oct 24	2.48	30	162425.01+295511.8[a]	2018 Jun 23	2.03	15
	2018 Sep 13	1.96	15		2017 Oct 25	2.00	10	165349.37+274647.3[a]	2018 Aug 14	1.61	15
	2018 Sep 14	0.71	10	084614.89+193515.3	2017 Dec 13	1.98	15		2018 Aug 15	3.34	15
020409.84+212948.5	2017 Jul 29	1.68	10	084953.09+105621.2	2019 May 08	2.09	10		2018 Aug 16	3.10	15
	2017 Jul 30	2.47	15		2019 May 09	2.26	10		2018 Oct 10	2.15	15
023402.50+243352.2	2017 Oct 23	2.29	20	092106.44+140736.7	2017 Dec 13	2.01	10		2018 Oct 11	2.21	15
	2017 Oct 26	1.38	30		2018 May 14	2.77	15	173232.09+335610.4[a]	2018 Jul 12	2.47	15
025352.96+332803.6[a]	2017 Dec 12	2.08	15		2018 May 16	1.91	15		2018 Jul 17	1.12	15
	2017 Dec 13	3.64	15	092355.26+085717.3	2019 Dec 15	2.54	20	174025.00+245705.5	2018 Jun 23	2.73	15
065146.31+271927.3	2017 Nov 22	2.12	15		2019 Dec 16	3.52	15		2018 Jun 24	4.15	15
	2017 Nov 23	1.46	10	101502.95+464835.3[a]	2018 Jan 24	2.89	10	183252.20+421526.1	2018 Jun 19	2.93	15
073935.14+244505.2[a]	2017 Oct 20	1.07	15	105423.94+211057.4	2018 Jan 23	3.17	10		2018 Jun 25	2.98	15
	2017 Oct 21	1.47	10		2018 Jan 28	2.52	10	212403.12+114230.2[a]	2018 Jun 20	2.79	15
074925.14+195040.0	2017 Nov 24	1.74	10	110235.85+623416.1[a]	2018 Mar 17	3.37	8		2018 Jun 21	3.10	15
	2017 Dec 13	1.46	15		2020 Jan 13	4.09	20		2018 Jun 22	3.31	10
075452.85+194907.0	2017 Dec 17	4.12	15	112752.92+553522.0	2017 May 21	3.13	15	214441.71+010029.8	2017 Jul 31	2.52	15
	2018 Jan 24	1.80	5		2017 May 23	1.67	15		2018 Aug 16	2.39	15
075523.86+172825.1	2017 Oct 21	1.24	15	113247.25+283519.0	2018 Mar 13	1.15	5	220250.26+213120.2	2017 May 23	1.08	15
	2017 Oct 22	1.96	15		2018 Mar 16	2.64	15		2017 May 24	1.67	20
080236.92+154813.6[a]	2017 Oct 26	1.91	20	131646.02+414639.0	2018 Mar 14	1.36	15	222833.82+141036.9	2017 Nov 23	2.74	15
	2018 Jan 23	2.09	10		2018 May 16	2.80	5		2017 Nov 24	2.07	10
080349.15+085532.6	2017 Nov 24	1.38	10	140028.43+475644.1	2017 Jun 24	2.19	30	225020.91−091425.6[a]	2018 Aug 15	4.82	15
	2017 Dec 12	1.40	15		2017 Jun 25	2.34	15	225424.73+231515.8[a]	2018 Jul 19	1.30	15
081345.42+365140.5[a]	2017 Dec 18	4.23	15	142405.54+181807.3	2019 May 01	2.62	15		2018 Jul 20	4.92	15
	2017 Dec 21	3.27	15		2019 May 02	3.91	15	232108.40+010433.5	2017 Nov 25	1.85	15
	2018 Jan 25	2.92	10		2017 Jun 26	1.32	30		2017 Dec 16	2.22	10
081453.55+300734.8[a]	2017 Nov 24	1.55	14	144814.33+150449.7	2017 Jun 27	3.14	10	232711.11+515344.7	2018 Sep 10	4.00	3
	2020 Jan 23	2.72	30	145755.43+015442.9	2017 May 19	1.78	10		2018 Sep 11	4.00	3
081656.17+204946.0	2017 Nov 22	1.92	20		2017 May 23	2.66	15		2018 Sep 12	3.01	3
	2017 Nov 25	1.78	20	151729.46+433028.6	2018 Jul 06	1.55	15	234848.77+381754.6	2017 Nov 23	1.86	5
	2017 Dec 12	1.28	10	153454.99+224918.6	2018 May 14	2.51	15		2017 Nov 24	1.03	3

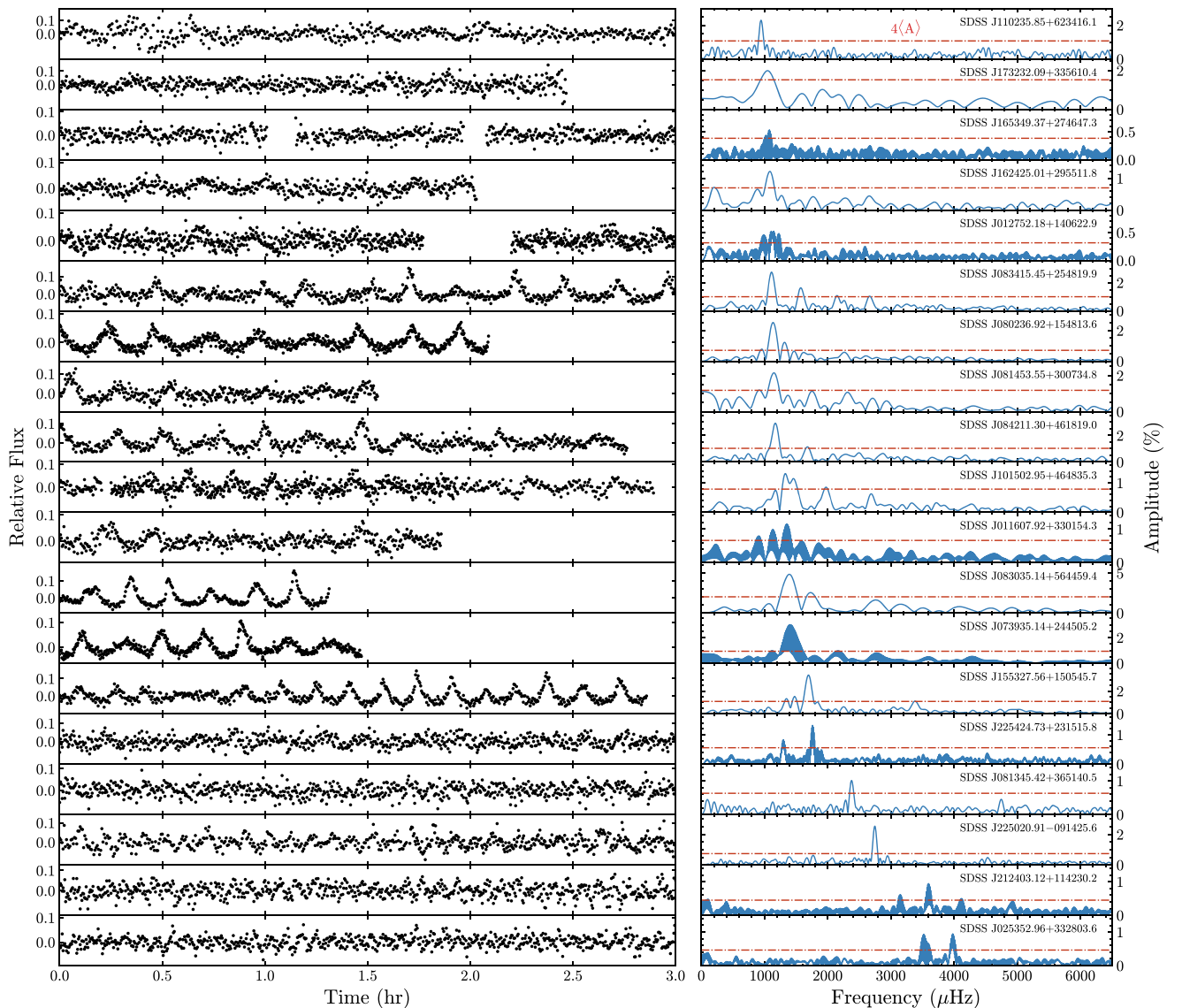**Note.**
[a] New DBVs from this work.

Figure 2. The light curves (left) and FTs (right) for each new DBV. Objects are ordered from top to bottom by increasing frequency (decreasing period) of the dominant observed mode. The $4\langle A\rangle$ significance threshold for each FT is shown with a horizontal red line. Some of the FTs are for multiple consecutive nights of observations, hence the higher density of peaks. Gaps in some light curves are caused by inclement weather.

a low-order polynomial of degree two or lower, and clipped any outliers or data heavily affected by clouds. Last, we used WQED to perform a barycentric correction of the mid-exposure time stamps of our images.

3. New DBVs and Limits on Variability

We observed a total of 55 DBs and DBAs with the McDonald 2.1 m telescope over the course of 270 total hours. We detected pulsations in 19 new DBVs, a success rate of about 35%, similar to that of Nitta et al. (2009). In Figure 2 we present the light curve for each newly discovered DBV, along with the associated Fourier transform (FT) calculated using the PERIOD04 program (Lenz & Breger 2004), ordered from top to bottom by increasing frequency of the dominant mode. In this section we characterize the DBVs, measuring their pulsation periods and amplitudes, and we also place limits on the variability for those objects that show no evidence for pulsations.

To identify significant pulsation modes, we first calculate FTs of our light curves using PERIOD04, oversampling the frequencies by a factor of 20. We then adopt an iterative prewhitening procedure similar to that described in Bell et al. (2017b), first assessing whether the highest peak in the FT rises above a $4\langle A\rangle$ threshold, where $\langle A\rangle$ is the average amplitude of the FT between 500 and 10,000 μHz ($4\langle A\rangle$ approximates a 0.1% false-alarm probability level for relatively short time-series observations; Breger et al. 1993; Kuschnig et al. 1997). If the peak is significant, we perform a nonlinear least-squares fit of a sinusoid to the light curve, using the peak frequency and amplitude as initial guesses. We then prewhiten the light curve by subtracting the best-fit sinusoid and calculating an FT of the residuals. We find the highest peak remaining and repeat the above process until no significant peaks remain, each time fitting a sum of sinusoids to the light curve.

For objects with multiple nights of observations, the gaps between runs introduce cycle count ambiguities that manifest as complex aliasing structures in the spectral window of the FT.

These aliasing structures make it difficult to identify the correct periods and allow for multiple viable period solutions (e.g., Bell et al. 2017a, 2018). To reduce the impact of aliasing on our determined periods, we only combine light curves for seven objects that were observed on consecutive nights, and otherwise use the highest-quality single-night light curve to characterize the periods. We only determine one period solution per object and report analytical least-squares uncertainties (Montgomery & Odonoghue 1999) for our frequencies, periods, and amplitudes. We stress, however, that for the seven objects with combined multinight light curves, the characteristic spacing between aliases of $\approx 11.6\ \mu$Hz (the inverse of one sidereal day) sets extrinsic errors on our frequencies that are much larger than the reported formal uncertainties.

In Table 2 we list the identified significant periods for each new DBV and assign them a preliminary mode ID, f_{ij}, where i is a unique number for each object, and j is a unique letter for each mode within the object (e.g., f_{1a}). We generate all possible additive combinations of the significant periods for each object, including harmonics. If any combinations match a significant frequency within the frequency resolution defined by the length of the light curve, we identify them as possible combination modes. Due to the low-frequency resolutions of our light curves, multiple combination possibilities often exist for many modes, and some might actually be independent modes, so we do not constrain any periods to exact arithmetic relations when fitting with PERIOD04. In the mode ID column of Table 3, we list only the combination we consider most likely, which is typically the combination involving the closest frequency match or the highest-amplitude parent modes.

For objects with multiple nights of data, the frequency resolution of the combined light curve is often much lower than the width of the spectral window, so in these cases we use the frequency resolution of the longest single-night light curve as the matching tolerance when searching for combinations. We also note that even for modes that are unlikely to be combinations, our observing runs are too short in most cases to resolve closely spaced modes or rotationally split multiplets, and more extensive observing would be needed to properly identify the independent pulsation modes in these objects. Still, throughout the analysis in this work, we treat any significant frequencies that are unlikely to be combinations as independent modes in these stars.

Objects that show no significant peaks during any of the nights observed are classified as NOV. We identified 36 new NOVs and used the $4\langle A \rangle$ thresholds of their FTs to place limits on their variability. Of the 36 objects, 34 (94%) were observed on at least two separate occasions. For these objects, we calculated NOV limits using their combined light curves, regardless of how many nights separated the observations. For 32 objects, 89% of our sample, we achieved NOV limits lower than 0.5% and reached an average limit of 3.3 mma for our full sample. We list the NOV limits along with the number of observing runs acquired for each object in the rightmost columns of Table 5 located in the Appendix.

White dwarfs are known to exhibit pulsation amplitudes below our NOV limits, and it is also possible that we observed some objects only during phases of destructive beating between pulsation modes. Additional observations may be needed for some objects to rule out pulsations with higher confidence, especially for DBs with $T_{\rm eff}$ near the blue edge, where pulsation amplitudes tend to be small. Still, our NOV limits represent an improved assessment of variability throughout the DB instability strip compared to Nitta et al. (2009), where only 15% of NOVs were observed on more than one night, and only 30% have NOV limits <5 mma, giving an average NOV limit of 8.9 mma. With our observations, we were also able to identify pulsations in one DB, SDSS J101502.95+464835.3, that was previously identified as an NOV by Nitta et al. (2009) with a variability limit of 7.2 mma using a single 1.7 hr run. We detected four independent pulsation modes in this object with amplitudes of 6.9–12.1 mma, indicating destructive beating was likely occurring during the observations of Nitta et al. (2009), and highlighting the need for more extensive observations to improve assessment of variability throughout the DB instability strip.

4. The DB/DBA Instability Strip

In this section we use our sample of new DBVs and NOVs alongside previously known DBVs to provide new constraints on the empirical limits of the DB/DBA instability strip, and compare with the most recent theoretical calculations. For the new DBVs and NOVs in our sample, we took their spectroscopic $T_{\rm eff}$ and $\log(g)$ values from KK15 and Kepler et al. (2019), who fit 1D white dwarf atmospheric models to SDSS spectra from DR10, DR12, and DR14. Their models employ the ML2/α version (Böhm & Cassinelli 1971; Tassoul et al. 1990) of the mixing-length theory (MLT; Böhm-Vitense 1958) to describe convective energy transport, with the mixing-length parameter α set to 1.25 as calibrated by Beauchamp et al. (1999) and Bergeron et al. (2011).

Only 10 of the 28 previously known DBVs are found in KK15 or Kepler et al. (2019). For the remaining 18 objects, we acquire the spectroscopic $T_{\rm eff}$, $\log(g)$, and [H/He] parameters from various works in the literature that are listed in Table 3, all of which use ML2/$\alpha = 1.25$. Three of these 18 objects, EC 05221−4725, WD J025121.71−125244.85, and WD J132952.63+392150.8, have not yet been spectroscopically analyzed, so we exclude them from our analysis. Thus, in the sections below, we analyze a total of 80 pulsating and NOV DB/DBAs.

The atmospheric models and fitting procedures differ in some ways between these works, but we opted for a complete rather than homogeneous sample so we could present a complete census of all currently known DBVs. Because of this inhomogeneity, some caution should be taken when interpreting the limits of the observed instability strip, which can vary based on which atmospheric models and fitting methods are used. One consistent factor, however, is that all the atmospheric parameters used in this work were calculated using the ML2/$\alpha = 1.25$ mixing-length prescription. This allows us to apply the 3D $T_{\rm eff}$ and $\log(g)$ corrections from Cukanovaite et al. (2021) later on to see how they might affect the empirical extent of the instability strip, and compare with spectroscopic and photometric parameters derived in separate works (e.g., Genest-Beaulieu & Bergeron 2019b; Gentile Fusillo et al. 2021).

With the exception of the two objects fit by Kleinman et al. (2013), all the works mentioned above consider the possibility of trace hydrogen in the atmospheres of the DBs they studied, and use the detection or nondetection of Hα to measure or place upper limits on [H/He] at the photosphere for each object. For all 19 new DBVs presented in this work, only upper limits on [H/He] have been determined, while 9 of the 36 new NOVs have detected H, making them DBAs. Only 4 of the

Table 2
Observed Periods and Amplitudes for New DBVs

Name (SDSS J)	Frequency (μHz)	Period (s)	Amp. (mma)	Mode ID	Name (SDSS J)	Frequency (μHz)	Period (s)	Amp. (mma)	Mode ID
011607.92+330154.3[a]	1357.2[0.6]	736.8[0.3]	10.3[1.1]	f_{1a}	083415.45+254819.9	1113.0[2.2]	898.5[1.8]	27.5[1.2]	f_{9a}
	892.4[0.9]	1120.5[1.1]	7.5[1.1]	f_{1b}		1576.7[3.7]	634.2[1.5]	16.3[1.2]	f_{9b}
	1147.9[0.9]	871.1[0.7]	6.9[1.1]	f_{1c}		2672.7[5.7]	374.2[0.8]	10.5[1.2]	$f_{9a}+f_{9b}$
012752.18+140622.9[a]	1107.2[0.7]	903.1[0.5]	4.7[0.6]	f_{2a}		2144.0[6.1]	466.4[1.3]	9.8[1.2]	$2f_{9a}$
	1137.9[0.6]	878.8[0.4]	5.6[0.6]	f_{2b}	084211.30+461819.0	1178.4[2.4]	848.6[1.7]	28.1[1.2]	f_{10a}
	979.2[0.8]	1021.2[0.8]	4.0[0.6]	f_{2c}		1669.5[5.8]	599.0[2.1]	11.6[1.2]	f_{10b}
	1229.0[0.8]	813.7[0.5]	3.8[0.6]	f_{2d}		1100.8[5.9]	908.5[4.8]	11.5[1.2]	f_{10c}
025352.96+332803.6[a]	3978.0[0.4]	251.38[0.03]	9.4[0.7]	f_{3a}	101502.95+464835.3	1325.5[4.5]	754.4[2.6]	12.1[1.0]	f_{11a}
	3519.4[0.5]	284.14[0.04]	8.3[0.7]	f_{3b}		1474.8[5.0]	678.1[2.3]	11.0[1.0]	f_{11b}
	3588.8[0.7]	278.64[0.06]	5.5[0.7]	f_{3c}		1983.1[6.5]	504.3[1.7]	8.4[1.0]	f_{11c}
073935.14+244505.2[a]	1410.1[0.2]	709.2[0.1]	31.2[0.8]	f_{4a}		1166.8[7.9]	857.1[5.8]	6.9[1.0]	f_{11d}
	1174.8[0.5]	851.2[0.4]	9.6[0.8]	f_{4b}		2688.0[8.5]	372.0[1.2]	6.5[1.0]	$2f_{11a}$
	2152.7[0.5]	464.5[0.1]	10.7[0.8]	f_{4c}	110235.85+623416.1	946.1[3.3]	1057.0[3.7]	22.9[2.0]	f_{12a}
	1630.6[0.6]	613.3[0.2]	8.5[0.8]	f_{4d}	155327.56+150545.7	1663.1[2.5]	601.3[0.9]	22.9[1.1]	f_{13a}
	2735.5[0.6]	365.6[0.1]	7.9[0.8]	$2f_{4a}$		1500.7[4.4]	666.4[2.0]	12.7[1.1]	f_{13b}
	3597.4[0.9]	278.0[0.1]	5.5[0.8]	$f_{4a}+f_{4c}$		3382.6[4.9]	295.6[0.4]	11.4[1.1]	$2f_{13a}$
	1773.9[0.8]	563.7[0.2]	6.6[0.8]	f_{4e}		1722.9[2.5]	580.4[0.8]	22.4[1.1]	f_{13c}
	3004.1[1.0]	332.9[0.1]	5.1[0.8]	$f_{4a}+f_{4d}$		1329.2[6.2]	752.4[3.5]	9.1[1.1]	f_{13d}
	4273.1[1.1]	234.0[0.1]	4.7[0.8]	$3f_{4a}$		1862.8[5.9]	536.8[1.7]	9.5[1.1]	f_{13e}
080236.92+154813.6	1166.4[1.3]	857.4[0.9]	35.5[0.6]	f_{5a}	162425.01+295511.8	1086.5[7.4]	920.4[6.3]	12.1[1.2]	f_{14a}
	1227.2[2.4]	814.9[1.6]	18.9[0.6]	f_{5b}	165349.37+274647.3[a]	1078.3[0.4]	927.4[0.3]	5.4[0.7]	f_{15a}
	2257.1[7.2]	443.0[1.4]	6.3[0.6]	$2f_{5a}$	173232.09+335610.4	1049.3[18.7]	953.0[17.0]	20.2[2.8]	f_{16a}
	1694.1[9.5]	590.3[3.3]	4.8[0.6]	f_{5c}	212403.12+114230.2[a]	3596.3[0.2]	278.06[0.01]	12.7[0.8]	f_{17a}
081345.42+365140.5	2378.9[4.0]	420.4[0.7]	10.1[1.1]	f_{6a}		3602.1[0.3]	277.62[0.02]	8.6[0.8]	f_{17b}
	4748.9[8.9]	210.6[0.4]	4.5[1.1]	$2f_{6a}$		3157.8[0.4]	316.67[0.04]	5.9[0.8]	f_{17c}
081453.55+300734.8	1150.5[8.2]	869.2[6.2]	21.4[1.8]	f_{7a}		4111.1[0.5]	243.24[0.03]	5.2[0.8]	f_{17d}
083035.14+564459.4	1384.7[2.5]	722.2[1.3]	47.7[1.0]	f_{8a}		4933.3[0.6]	202.71[0.02]	4.2[0.8]	f_{17e}
	1763.9[5.4]	566.9[1.7]	21.8[1.0]	f_{8b}	225020.91−091425.6	2747.1[1.4]	364.0[0.2]	25.3[1.2]	f_{18a}
	2761.7[6.4]	362.1[0.8]	18.3[1.0]	$2f_{8a}$	225424.73+231515.8[a]	1761.3[0.2]	567.8[0.1]	13.6[0.9]	f_{19a}
	3160.0[9.8]	316.5[1.0]	12.0[1.0]	$f_{8a}+f_{8b}$		1301.0[0.3]	768.6[0.2]	8.9[0.9]	f_{19b}
	4127.3[12.6]	242.3[0.7]	9.3[1.0]	$3f_{8a}$					
	4553.3[16.5]	219.6[0.8]	7.1[1.0]	$2f_{8a}+f_{8b}$					
	5486.5[18.5]	182.3[0.6]	6.3[1.0]	$4f_{8a}$					

Note. Uncertainties are given in brackets next to each value. For combination modes, multiple possibilities often exist within the frequency resolution of our light curves. We list here the option we consider most likely based on the frequency match and parent amplitudes.

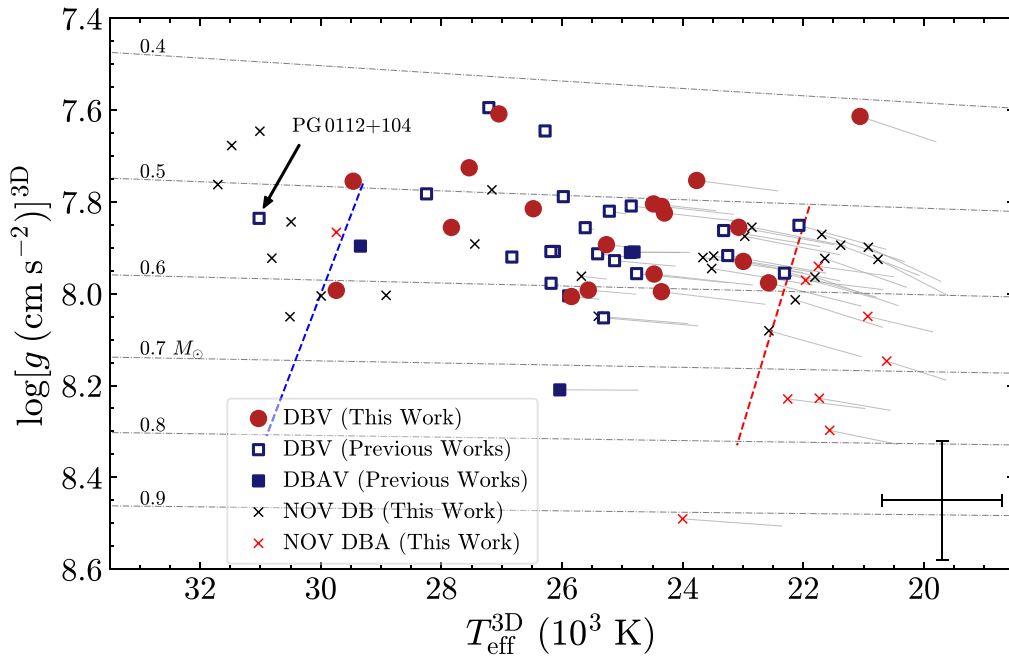[a] Indicates objects that were observed on two or more consecutive nights.

Figure 3. The DB/DBA instability strip with 3D $T_{\rm eff}$ and $\log(g)$ corrections from Cukanovaite et al. (2021) applied. Lines drawn from each point indicate the change from 1D spectroscopic $T_{\rm eff}$ and $\log(g)$ values, and a typical error-bar size is shown in the bottom right corner. In comparison with the theoretical blue and red edges from Van Grootel et al. (2017; dashed blue and red lines, respectively), the observed blue edge defined by PG 0112+104 is still significantly hotter, while the observed red edge appears just slightly hotter. As shown in Figure 5, however, the observed red edge can move significantly between studies using different model atmospheres and fitting methods.
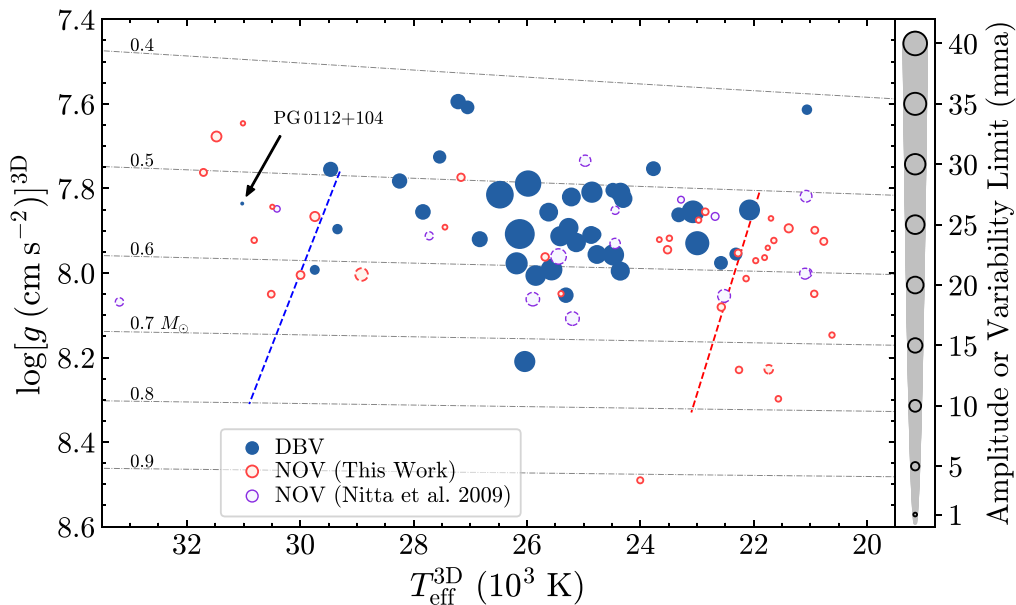
Figure 4. The same DB/DBA instability strip as in Figure 3, but with DBVs (blue circles) sized according to the amplitude of their dominant mode, and NOVs (open red and purple circles) sized according to their variability limit. Open red circles are new NOVs from this work, while open purple circles are NOVs from Nitta et al. (2009). Dashed vs. solid marker edges for NOVs indicate whether they were observed on one or more than one night, respectively. Our NOV limits are generally much lower than the typical pulsation amplitudes of DBVs, except near the blue edge where the measured pulsation amplitudes are often $\lesssim$5 mma (e.g., the highest-amplitude mode in PG 0112+104 is <0.3 mma, Hermes et al. 2017a). Four of the new NOVs in our sample have $T_{\rm eff}$ and $\log(g)$ more than 1σ inside the theoretical instability strip, all of which have two or more nights of observations and variability limits <5 mma (see Table 5).

previously known DBVs are classified as DBAs (Giammichele et al. 2018; Rolland et al. 2018).

We list the atmospheric properties for all new DBVs and NOVs in the Appendix in Tables 4 and 5, respectively. The $T_{\rm eff}$ and $\log(g)$ uncertainties for new DBVs and NOVs are the formal values from KK15 and Kepler et al. (2019), with 3.1% relative $T_{\rm eff}$ and 0.12 dex $\log(g)$ added in quadrature to account

for external uncertainties estimated by KK15. These are similar to the uncertainties estimated by Genest-Beaulieu & Bergeron (2019b) for their SDSS spectroscopic sample. For previously known DBVs, we use the uncertainties quoted by the same works where we obtained the atmospheric parameters.

Last, prior to investigating the observational extent of the DB/DBA instability strip, we apply the 3D $T_{\rm eff}$ and $\log(g)$
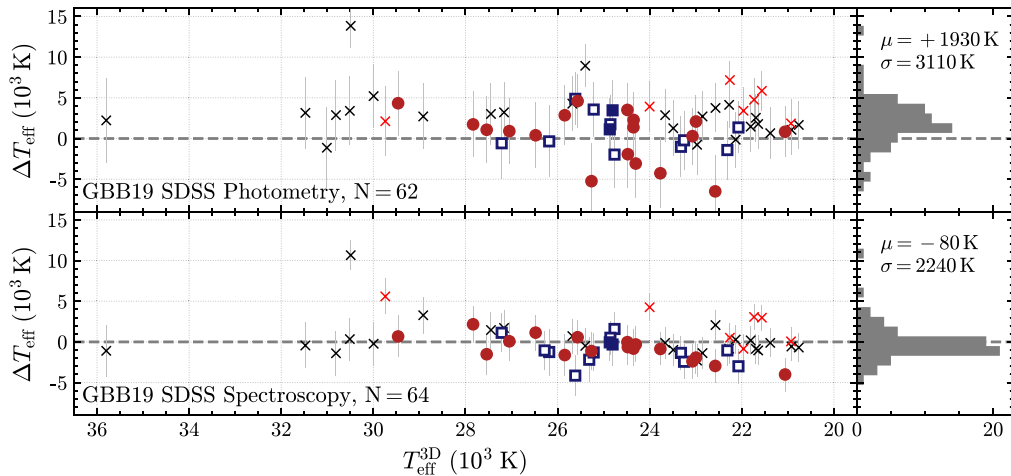
Figure 5. $T_{\rm eff}$ differences between those used in this work (see Tables 2, 4, and 5) and those provided by GBB19, who use SDSS photometry (top, 62 objects in common) and spectroscopy (bottom, 64 objects in common). $\Delta T_{\rm eff} = T_{\rm eff}^{\rm Our\ Sample} - T_{\rm eff}^{\rm GBB19}$ and 3D corrections have been applied to all spectroscopic parameters in this figure. Histograms of the $T_{\rm eff}$ differences are shown on the right along with their averages (μ) and root-mean-square deviations (σ). While the average spectroscopic $\Delta T_{\rm eff}$ for the full sample is negligible compared to the uncertainties in $T_{\rm eff}$, the spectroscopic parameters from GBB19 for DBVs below 24,000 K appear to be higher on average and would suggest a hotter red edge. The photometric parameters are systematically lower, but there is a larger amount of scatter. A few NOVs within our instability strip are also moved outside the instability strip according to the GBB19 spectroscopic or photometric parameters.

corrections calculated by Cukanovaite et al. (2021) to all of the new and previously known DBVs and NOVs. For DBs with only upper limits on [H/He], we perform the corrections using the lowest possible H-abundance in the Cukanovaite et al. (2021) grid, [H/He] = −10. Otherwise, we use the measured [H/He] values from the literature as input to the correction functions. The corrections for our sample of objects are almost negligible at temperatures above 26,000 K, but below this temperature, the corrections change the 1D $T_{\rm eff}$ and $\log(g)$ by about +1200 K and −0.03 dex on average.

In Figure 3 we show the updated DB/DBA instability strip after the application of 3D corrections. To indicate the direction and magnitude of the 3D corrections, we draw vectors from each point back to their respective 1D $T_{\rm eff}$ and $\log(g)$. The 3D corrections move nearly every DBV whose 1D atmospheric parameters are cooler than the theoretical red edge inside the theoretical instability strip of Van Grootel et al. (2017). Many NOVs move inside the instability strip as well, but most of them are still within the 1σ uncertainties of both the theoretical red edge and the coolest DBVs, and could conceivably be nonpulsators beyond the red edge. Overall, the 3D corrections appear to improve the agreement between the empirical and theoretical red edges, although potentially the theoretical red edge is still slightly too cool given that all the known cool DBVs are located inside the strip, and statistically, there ought to be some NOVs beyond the theoretical red edge given their large temperature uncertainties. The eight coolest DBVs in our observed instability strip are on average 650 K hotter than the theoretical red edge.

To date, PG 0112+104 is still the hottest known DBV (Hermes et al. 2017a) with $T_{\rm eff} = 31,040 \pm 1060$ K (Rolland et al. 2018), although we do find two new DBVs that are now the second and third hottest DBVs according to their spectroscopic $T_{\rm eff}$, SDSS J012752.18+140622.9 ($T_{\rm eff}^{\rm 3D} = 29,740 \pm 970$ K) and SDSS J212403.12+114230.2 ($T_{\rm eff}^{\rm 3D} = 29,460 \pm 1140$ K). Alongside KIC 8626021 (Bischoff-Kim et al. 2014; Giammichele et al. 2018), these help place additional constraints on the blue (hot) edge of the instability strip. We do note, however, that the detected pulsation periods of SDSS J012752.18+140622.9 are

relatively long, between 810 and 1020 s, which are more typical of cool-edge pulsators and call the accuracy of the atmospheric parameters for this object into question. We discuss this object further in Section 5. Meanwhile, PG 0112+104 still poses a significant challenge to the current theoretical blue edge from Van Grootel et al. (2017), who predict driving to begin around 29,500 K at $\log(g) = 7.8$. A higher convective efficiency (higher α) is still required to bring the observed and theoretical blue edges into agreement.

We also find several NOVs inside the instability strip. In Figure 4 we show the same instability strip as Figure 3, but size each DBV marker according to the amplitude of the dominant mode and each NOV marker according to the variability limit. We include the Nitta et al. (2009) sample of NOVs in this figure for a comparison of the variability limits of our samples, which is also described in the text at the end of Section 3. As shown in Figure 4, the majority of our NOVs and some of the NOVs from Nitta et al. (2009) have variability limits well below the typical measured pulsation amplitudes of DBVs at similar $T_{\rm eff}$ and $\log(g)$, except near the blue edge, where the measured pulsation amplitudes are often lower than our typical detection thresholds of 2–5 mma. Pulsation modes in PG 0112 +104, the hottest known DBV, reach only 0.3 mma amplitude in the Kepler bandpass (Hermes et al. 2017b).

Due to the large temperature uncertainties in these objects, some NOVs may in fact belong outside the instability strip, but some objects remain well within the instability strip even when using atmospheric parameters from different studies. In particular, four objects in our NOV sample have multiple nights of observations and NOV limits below 5 mma and reside near the middle of the instability strip and more than 1σ away from both the blue and red theoretical edges. SDSS J081656.17+204946.0, for example, with an NOV limit from three nights of photometry of 1.73 mma, has $T_{\rm eff} = 27,400$ and $\log(g) = 7.89$ (KK15, SDSS spectroscopy), $T_{\rm eff} = 25,700$ and $\log(g) = 8.00$ (Genest-Beaulieu & Bergeron 2019b, SDSS spectroscopy), and $T_{\rm eff} = 24,400$ and $\log(g) = 8.08$ (Genest-Beaulieu & Bergeron 2019b, SDSS photometry), all of which place this object well within the instability strip. Most of the NOVs in our sample within the instability strip were observed on two separate nights, decreasing
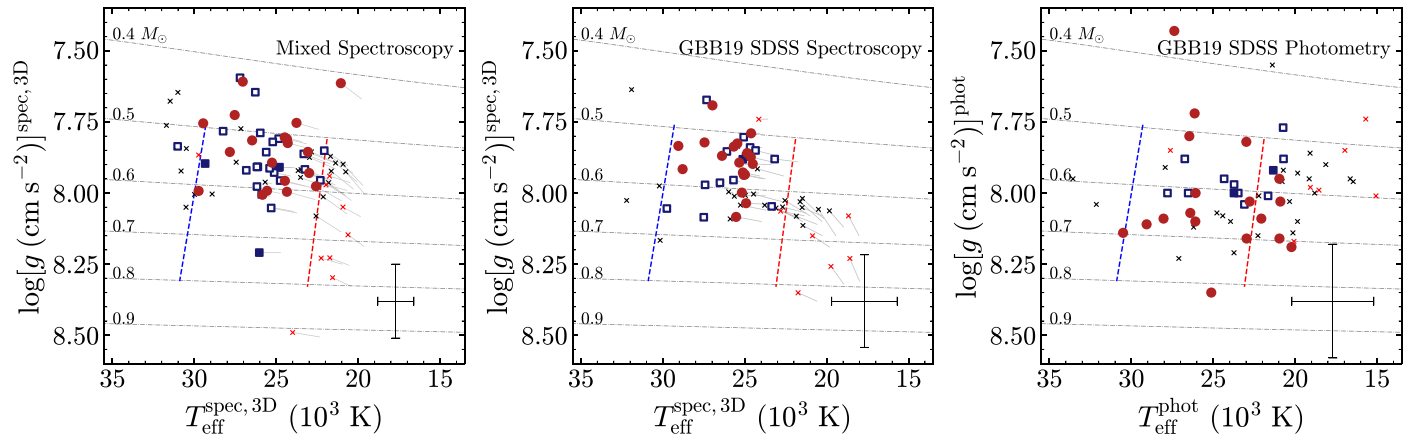
Figure 6. The instability strips generated using atmospheric parameters from different studies and fitting methods. On the left is the same instability strip from Figure 3, which uses an inhomogeneous set of spectroscopic parameters from a wide range of studies (see Tables 2, 4, and 5), but includes the largest number of known pulsating and NOV DBs and DBAs (80 objects). In the middle and right panels are instability strips generated from GBB19 spectroscopic (64 objects) and photometric (62 objects) parameters, respectively, which rely solely on SDSS observations. The symbol shapes and colors are the same as Figure 3, and we again use lines connected to each object with spectroscopic parameters to indicate the change from 1D T_{eff} and $\log(g)$ values. A typical error-bar size is shown in the bottom right corner of each panel, with the photometric parameters having notably larger uncertainties. The observed red edge changes by about ± 2000 K between different studies and fitting methods. The observed blue edge appears more stable, but is harder to define given the small number of objects, especially because the hottest known DBV, PG 0112+104, is only present in the left panel.

the chance that we caught them during cycles of destructive beating between modes, but such an effect may still account for some NOVs inside the instability strip, especially those in the Nitta et al. (2009) sample, which in most cases have only one night of observations. To place stronger upper limits on variability, especially near the blue edge, more extensive time-series photometry of these objects is required.

Even though we double the number of cool DBVs within 2000 K of the red edge from four to eight, the exact location of the observed red edge is still difficult to determine with our sample given the large temperature uncertainties and that the atmospheric parameters used here represent an inhomogeneous spectroscopic sample. Temperatures and surface gravities can vary by large amounts for single objects due to different atmospheric models, fitting routines, and properties of the observational data such as S/N, resolution, and wavelength coverage. To illustrate this, we show in Figure 5 the difference in T_{eff} and $\log(g)$ for our sample of DBVs and NOVs and those in common with the spectroscopic and photometric analyses of Genest-Beaulieu & Bergeron (2019b).

Genest-Beaulieu & Bergeron (2019b; abbreviated GBB19 hereafter), use both SDSS spectroscopy and photometry from DR12 and earlier to determine two independent sets of temperatures and surface gravities for their objects, one set based on the spectroscopic method, and the other set based on the photometric method. Out of the 80 objects in our sample with prior spectroscopic observations, we find 64 objects in GBB19 with SDSS spectroscopy, and 62 objects with SDSS *ugriz* photometry. Unsurprisingly, given that most of our atmospheric parameters come from KK15, who also use SDSS spectra from DR12 and below, the T_{eff} and $\log(g)$ we use in this work agree closely with the spectroscopic analysis of GBB19.

For the 64 objects in GBB19 with spectroscopic parameters, the T_{eff} and $\log(g)$ of our sample are 80 K cooler and 0.05 dex lower than the GBB19 values, with rms deviations of 2200 K and 0.10 dex. Despite the small average difference in T_{eff}, the coolest DBVs in our sample with $T_{\mathrm{eff}} \lesssim 24{,}000$ K have systematically lower T_{eff} than the spectroscopic sample of GBB19, which would produce a red edge that is about 2000 K hotter. We show this effect more clearly in the middle

panel of Figure 6, which displays the DB instability strip as defined by the spectroscopic parameters from GBB19. After 3D corrections are applied, only two DBVs have T_{eff} lower than 24,000 K, and the majority of DBVs are clumped around 25,000 K. This clumping effect is primarily caused by the 3D spectroscopic corrections, but even without 3D corrections, the coolest DBVs in GBB19 would still be systematically hotter than our inhomogeneous sample.

For the 62 objects in GBB19 with photometric parameters, the average T_{eff} for our 3D-corrected spectroscopic sample is actually 1900 K hotter than the GBB19 values, although the amount of scatter is significantly larger, with rms deviations around 3100 K. This effect can again be seen more clearly in the right panel of Figure 6, where a much larger number of DBVs and DBAVs is seen at temperatures cooler than the proposed theoretical red edge of Van Grootel et al. (2017) than in either of the spectroscopic samples. In this case, however, the difference between our sample of spectroscopic parameters and the photometric parameters of GBB19 near the red edge would actually be greatly reduced without the application of 3D spectroscopic corrections, although the photometric parameters are still about 1000 K cooler on average for the whole sample.

As seen in Figure 6, while the red edge can vary by about ± 2000 K between the different studies and fitting methods, the effect on the blue edge is much harder to determine due to the low number of hot DBVs. It appears to be somewhat more stable than the red edge, but unfortunately, the hottest known DBV, PG 0112+104, does not fall within the SDSS footprint and so is not contained in the GBB19 sample. At least one hot DBV is always found near to the theoretical blue edge between the different studies and methods, although perhaps a more systematic drop in T_{eff} can be seen in the photometric sample than in the spectroscopic sample.

We also attempted to compare the atmospheric parameters for our sample of DBVs and NOVs with those determined by Gentile Fusillo et al. (2021). They use the photometric method with Gaia eDR3 photometry and parallax to derive T_{eff} and $\log(g)$ assuming either a pure-H, pure-He, or mixed H–He atmosphere with $[\mathrm{H/He}] = -5$. The Gaia photometry,

Name	Spectroscopy	Pulsation Periods
SDSS J034153.03−054905.9	Koester & Kepler (2015)	Nitta et al. (2009)
SDSS J094749.40+015501.9	Kleinman et al. (2013)	Nitta et al. (2009)
SDSS J104318.45+415412.5	Kleinman et al. (2013)	Nitta et al. (2009)
SDSS J122314.25+435009.1	Koester & Kepler (2015)	Nitta et al. (2009)
SDSS J125759.04−021313.4	Kepler et al. (2019)	Nitta et al. (2009)
SDSS J130516.51+405640.8	Koester & Kepler (2015)	Nitta et al. (2009)
SDSS J130742.43+622956.8	Koester & Kepler (2015)	Nitta et al. (2009)
SDSS J140814.64+003839.0	Kepler et al. (2019)	Nitta et al. (2009)
EC 01585−1600	Rolland et al. (2018)	Bell et al. (2019)
EC 04207−4748	Koester et al. (2014)	Kilkenny et al. (2009)
EC 05221−4725	⋯	Kilkenny et al. (2009)
KUV 05134+2605	Rolland et al. (2018)	Bognár et al. (2014)
CBS 114	Rolland et al. (2018)	Handler et al. (2002)
PG 1115+158	Rolland et al. (2018)	Winget et al. (1987)
PG 1351+489	Rolland et al. (2018)	Redaelli et al. (2011)
PG 1456+103	Rolland et al. (2018)	Handler et al. (2002)
GD 358	Rolland et al. (2018)	Provencal et al. (2009)
PG 1654+160	Rolland et al. (2018)	Handler et al. (2003)
PG 2246+121	Rolland et al. (2018)	Handler (2001)
EC 20058-5234	Koester et al. (2014)	Sullivan et al. (2008)
PG 0112+104	Rolland et al. (2018)	Hermes et al. (2017a)
KIC 8626021	Giammichele et al. (2018)	Østensen et al. (2011)
EPIC 228782059	Kepler et al. (2019)	Duan et al. (2021)
SDSS J085202.44+213036.5	Koester & Kepler (2015)	Nitta et al. (2009)
WD J025121.71−125244.85	⋯	Rowan et al. (2019)
SDSS J102106.69+082724.8	Koester & Kepler (2015)	Rowan et al. (2019)
SDSS J123654.96+170918.7	Koester & Kepler (2015)	Rowan et al. (2019)
WD J132952.63+392150.8	⋯	Rowan et al. (2019)

however, is not well suited for measuring the temperatures of hot objects given its broad and relatively red passbands, with average uncertainties of about 4500 K and 0.26 dex in $T_{\rm eff}$ and $\log(g)$ for our sample of objects. These uncertainties prevent any meaningful comparison between the atmospheric parameters of our sample, but at the very least, we do not find any significant systematic differences in $T_{\rm eff}$ or $\log(g)$ in comparison with Gentile Fusillo et al. (2021).

Although we have increased the number of DBVs, we have not found pulsations in any new objects with detected trace H. We have placed NOV limits on nine new DBAs, all of which lie beyond the theoretical red edge after 3D corrections, but their small number still prevents any definitive claim about whether the DBA instability strip occurs at lower temperatures than the pure-He DB instability strip. Considerable effort is required to find more of these objects.

5. Pulsation Properties of the DBVs

Pulsations in DBVs, just like their H-atmosphere DAV counterparts, are gravity modes excited by the convective driving mechanism (Brickhill 1991; Wu & Goldreich 1999). Driving is strongest for pulsation modes whose periods are about 25 times the thermal timescale at the base of the convection zone (Goldreich & Wu 1999), which becomes longer as white dwarfs cool monotonically through the instability strip and the convection zone deepens. Observed pulsation periods vary between about 2 minutes near the hot edges of both the DA and DB instability strips to about 20 minutes near the cool edges. The ensemble properties of DAVs, in particular how the observed pulsation modes evolve from short to long periods as a function of decreasing $T_{\rm eff}$, have been investigated for decades (Robinson 1979; McGraw 1980; Winget & Fontaine 1982; Clemens 1993, 1994; Mukadam et al. 2006), with more recent works using K2 observations of DAVs

(Hermes et al. 2017b), homogeneous spectroscopic samples (Fuchs 2017), and searches for DAVs in the Gaia survey (Vincent et al. 2020) showing similar trends of period versus $T_{\rm eff}$.

With the relatively small number of DBVs known prior to this work and the large uncertainties in their effective temperatures, the ensemble pulsation properties of DBVs have yet to be investigated in great detail. While they ought to mirror those of DAVs given the similarity in driving mechanism, some complicating factors exist, such as the presence of trace atmospheric H, which can have a systematic effect on $T_{\rm eff}$. In this section, we characterize the pulsation properties of all DBVs by investigating how both the periods and amplitudes of the observed pulsation modes vary as a function of $T_{\rm eff}$.

A common metric used to characterize the observed pulsations in white dwarfs is the weighted mean period (WMP; Clemens 1993), defined as WMP $= \sum_i A_i P_i / \sum_i A_i$, where each measured pulsation period, P_i, is summed while being weighted by its associated amplitude, A_i. Mukadam et al. (2006) showed that the WMP for DAVs exhibits a roughly linear trend with $T_{\rm eff}$ with a slope of -0.83 ± 0.08 s K^{-1}, although more detailed studies with a larger number of homogeneously characterized DAVs (Fuchs 2017) show a more piece-wise linear trend, with WMP first increasing more slowly between the blue edge and $T_{\rm eff} \simeq 12,000$ K. Regardless of the exact trend, the WMP is a model-independent quantity that is much easier to measure with high precision than $T_{\rm eff}$ and $\log(g)$, making it an attractive parameter with which to map properties of DBVs throughout the instability strip given their large $T_{\rm eff}$ uncertainties. We calculate the WMP for each of the new DBVs using the periods summarized in Table 3, and for the known DBVs, using periods identified in the literature (see references in Table 2). When calculating the WMP, we use only the independent pulsation modes, ignoring any frequencies likely to be linear combinations or harmonics. For each object, we also keep track of the period of the highest-amplitude mode, $P_{\rm max}$, as a separate but similar metric that may exhibit a trend with $T_{\rm eff}$.

We list the WMP and $P_{\rm max}$ values for each new DBV identified in this work in Table 4, and in Figure 7 we plot both the WMP and $P_{\rm max}$ versus the 3D-corrected effective temperatures. The parameters show similar trends, increasing as a function of decreasing effective temperature. Linear trends fit to both the WMP and $P_{\rm max}$ data have nearly identical slopes, with equations of WMP $= -0.087^{\pm 0.014} T_{\rm eff}^{\rm 3D} + 2840^{\pm 360}$ and $P_{\rm max} = -0.091^{\pm 0.015} T_{\rm eff}^{\rm 3D} + 2940^{\pm 370}$, respectively. Compared to the slope measured by Mukadam et al. (2006) for DAVs, the WMP for DBVs exhibits a much more gradual increase with decreasing $T_{\rm eff}$. This is expected, as the thermal timescale at the base of the convection zone, $\tau_{\rm th}$, has a much weaker dependence on $T_{\rm eff}$ for DBVs ($\tau_{\rm th} \propto T_{\rm eff}^{-20}$) than for DAVs ($\tau_{\rm th} \propto T_{\rm eff}^{-90}$; Goldreich & Wu 1999; Wu 2001; Montgomery 2005).

Unfortunately, using the above equations to translate a WMP or $P_{\rm max}$ value into an effective temperature is still fraught with difficulty. Even though the WMP values are model independent, the linear trends are not because they depend on the atmospheric models, fitting procedures, and data that were used to derive $T_{\rm eff}$. For example, if we repeat the fitting process using only DBVs with spectroscopic parameters from Genest-Beaulieu & Bergeron (2019b), the WMP and $P_{\rm max}$ equations then become WMP $= -0.108^{\pm 0.021} T_{\rm eff}^{\rm 3D} + 3460^{\pm 530}$ and $P_{\rm max} = -0.112^{\pm 0.021} T_{\rm eff}^{\rm 3D} + 3580^{\pm 550}$, respectively. The steeper trends are caused by many of the coolest DBVs in our sample having systematically higher $T_{\rm eff}$ determinations in Genest-Beaulieu & Bergeron (2019b). Still, the similarities in

Table 4
Atmospheric Parameters and Pulsation Properties for New DBVs

Name (SDSS J)	Type	P-M-F	g (mag)	$T_{\rm eff}$ (K)	$\log(g)$ (cgs)	$T_{\rm eff}^{\rm 3D}$ (K)	$\log(g)^{\rm 3D}$ (cgs)	WMP (s)	$P_{\rm max}$ (s)
011607.92+330154.3	DBV	6594-56272-971	18.9	21040[760]	8.03[0.13]	22580	7.98	890.7[0.6]	736.8[0.6]
012752.18+140622.9	DBV	4665-56209-726	18.3	29760[970]	7.99[0.13]	29740	7.99	903.1[0.5]	903.1[0.7]
025352.96+332803.6	DBV	2398-53768-185	18.8	27560[920]	7.72[0.13]	27540	7.73	269.6[0.2]	251.4[0.2]
073935.14+244505.2	DBV	4470-55587-626	17.3	21500[700]	7.89[0.12]	23070	7.86	663.4[0.3]	709.2[0.3]
080236.92+154813.6	DBV	4494-55569-174	17.4	21400[690]	7.97[0.12]	22990	7.93	822.3[0.9]	857.4[1.0]
081345.42+365140.5	DBV	2674-54097-287	18.8	27060[950]	7.61[0.13]	27050	7.61	420.4[0.9]	420.4[0.8]
081453.55+300734.8	DBV	930-52618-565	18.7	22630[940]	8.02[0.13]	24350	8.00	869.2[2.5]	869.2[2.5]
083035.14+564459.4	DBV	1783-53386-540	17.3	26490[850]	7.82[0.12]	26480	7.81	673.5[1.0]	722.2[1.1]
083415.45+254819.9	DBV	1930-53347-357	18.3	22850[960]	7.98[0.13]	24470	7.96	799.9[1.1]	898.5[1.3]
084211.30+461819.0	DBV	763-52235-435	18.5	24780[880]	8.00[0.13]	25570	7.99	805.3[1.2]	848.6[1.3]
101502.95+464835.3	DBV	944-52614-328	18.6	23460[810]	7.82[0.13]	24480	7.80	696.3[1.2]	754.4[1.6]
110235.85+623416.1	DBV	2882-54498-20	17.7	23160[760]	7.83[0.12]	24350	7.81	1057.0[1.9]	1057.0[1.9]
155327.56+150545.7	DBV	2521-54538-276	18.1	24720[900]	7.90[0.13]	25260	7.89	616.0[0.8]	601.3[0.9]
162425.01+295511.8	DBV	4953-55749-422	18.0	22430[780]	7.78[0.13]	23770	7.75	920.4[2.5]	920.4[2.5]
165349.37+274647.3	DBV	1690-53475-637	18.7	19800[680]	7.67[0.14]	21060	7.61	927.4[0.6]	927.4[0.6]
173232.09+335610.4	DBV	2262-54623-450	19.3	23010[1000]	7.84[0.14]	24300	7.82	953.0[4.1]	953.0[4.1]
212403.12+114230.2	DBV	730-52466-380	19.0	29480[1140]	7.75[0.15]	29460	7.75	270.6[0.1]	278.1[0.1]
225020.91-091425.6	DBV	724-52254-341	18.8	25390[1240]	8.01[0.14]	25840	8.01	364.0[0.4]	364.0[0.4]
225424.73+231515.8	DBV	6308-56215-843	19.0	27850[950]	7.85[0.13]	27830	7.86	647.1[0.3]	567.8[0.3]

Note. All new DBVs have only upper limits on [H/He] from KK15 or Kepler et al. (2019). 3D corrections were calculated assuming [H/He] = −10.
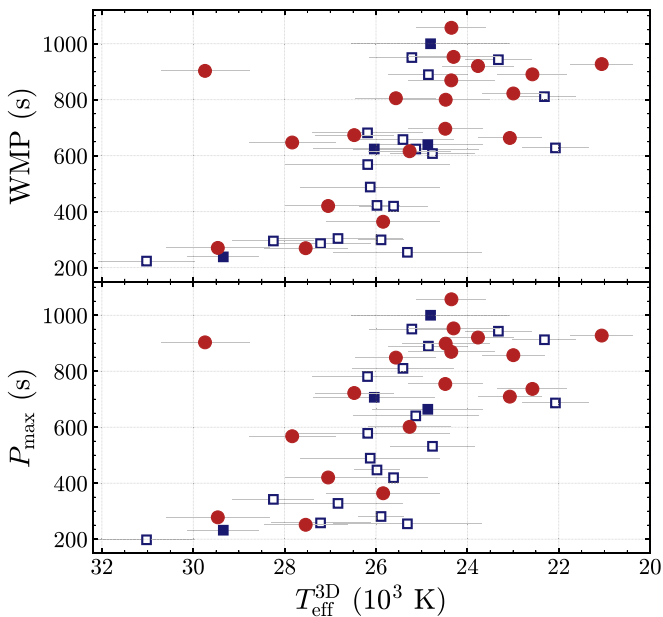

Figure 7. The WMP (top panel) and highest-amplitude period ($P_{\rm max}$, bottom panel) vs. the 3D-corrected effective temperatures for each new (red circles) and previously known (blue squares) DBV. No harmonics or combination frequencies were used to calculate the WMP. Periods and amplitudes for previously known DBVs were taken from the literature. Both show mild trends of increasing period with decreasing effective temperature, similar to the trend observed for DAVs (Robinson 1979; McGraw 1980; Clemens 1993; Mukadam et al. 2006; Fuchs 2017; Hermes et al. 2017b; Vincent et al. 2020). Here and in Figure 8, we adopt the Kepler et al. (2019) spectroscopic solution for EPIC 228782059 ($T_{\rm eff}$ = 28, 260 K), but cool solutions between 21,000 and 22,000 K have also been proposed based on both spectroscopic and asteroseismic modeling (Koester & Kepler 2015; Duan et al. 2021).

the trends even when using atmospheric parameters from different studies suggest that the WMP, just like for DAVs, is a good proxy for $T_{\rm eff}$ and can be used to investigate other trends throughout the instability strip, such as the pulsation power.

As mentioned in Section 4, we find one of the new DBVs, SDSS J012752.18+140622.9, to be a significant outlier, having a relatively long WMP of 903.1 ± 0.5 s, but a 3D effective temperature of 29, 740 ± 970 K placing it near the blue edge (the object has a photometric fit from Gentile Fusillo et al. 2021 using Gaia eDR3 photometry of 27, 440 ± 7900 K). The WMP suggests that this object is much cooler, with most DBVs near this period having $T_{\rm eff}$ between 22,000 and 25,000 K. As mentioned previously, DBVs often have degenerate hot and cool solutions centered on the middle of the instability strip due to the insensitivity of He I lines to changes in $T_{\rm eff}$ in this region, so it is possible for this object to in fact be a cool DBV whose hot solution was slightly preferred during the fitting process. In KK15 and Kepler et al. (2019), photometric fits to SDSS $ugriz$ were used to choose between degenerate hot and cool spectroscopic solutions. The cool solution for this object gives a 3D-corrected effective temperature of 21,260 K. Another possibility is that this object might be an unresolved double degenerate, which can produce unreliable temperature determinations. The Gaia eDR3 photometry and parallax suggest that this system might be overluminous, but with low confidence given the large relative parallax uncertainty of 42%.

Another notable object within the WMP diagram is EPIC 228782059, a DBV that was observed during $K2$ campaign 10 and recently proposed as possibly the coolest known DBV based on spectroscopic and asteroseismic analyses (Duan et al. 2021). In KK15, the best-fit spectroscopic model occurs at $T_{\rm eff}$ = 20,900 K and $\log(g)$ = 7.91, while in Duan et al. (2021), the best-fit asteroseismic model occurs at $T_{\rm eff}$ = 21,900 K and $\log(g)$ = 7.94, both consistent with EPIC 228782059 being a cool DBV. Using the list of pulsation periods reported in Duan et al. (2021), however, this object has a WMP of 295 s, which as a cool DBV would make it a rather severe outlier in our WMP diagram. Similar outliers have also been found among the DAVs without a definitive explanation (Mukadam et al. 2004; Fuchs 2017; Vincent et al. 2020), although an unresolved double degenerate is again one possibility. This object, however, was also included in the analyses of both Kong et al. (2018) and Kepler et al. (2019), who, when fitting the same SDSS spectrum as KK15, find that hotter solutions between 28,000 and 30,000 K are preferred. As

noted by Duan et al. (2021), these hotter solutions translate into luminosity distances that disagree with the distance derived from the Gaia eDR3 parallax (Bailer-Jones et al. 2021), thus favoring the cooler solutions. We adopt the hotter solution for this object from Kepler et al. (2019) in Figures 7 and 8, but note that there is still considerable ambiguity about the temperature of this object.

Following the analysis of Mukadam et al. (2006) for the DAVs, we also attempt to measure the power contained within the observed pulsation modes for all of the known DBVs. Measuring the intrinsic amplitudes of pulsation modes is a much more difficult task, however, than measuring the pulsation periods, and we stress here that we are not using a homogeneous set of observations for these measurements. Pulsation amplitudes are wavelength dependent, so observations in different filters will affect the measured amplitudes. Also, in our relatively short McDonald runs, any closely spaced modes from successive radial overtones or rotational splittings will remain unresolved and beat with one another, producing amplitudes that are higher or lower than if they were resolved. Periods and amplitudes for several previously known DBVs, however, come from extensive observations using the Whole Earth Telescope, the Kepler spacecraft, and the Transiting Exoplanet Survey Satellite (TESS), which are able to resolve closely spaced modes that single-night McDonald runs cannot.

Even in the absence of observational limitations, the intrinsic amplitudes remain difficult to determine due to geometric cancellation caused by disk averaging, the inclination angle of the white dwarf, and limb darkening. Pulsations in white dwarfs produce temperature variations on the surface that can be described using spherical harmonics (Robinson et al. 1982), with indices ℓ and m describing the number and distribution of pulsation nodes across the surface of the star. Modes with higher ℓ exhibit a larger number of bright and dark regions that, when averaged over the disk of the white dwarf, experience more cancellation. The inclination of the white dwarf determines the distribution of bright and dark spots that fall within our field of view for a given mode, while limb darkening reduces the amount of flux coming from the edges of the stellar disk. Disk averaging and the inclination angle will always serve to reduce the measured amplitude with respect to the intrinsic amplitude, although limb darkening actually boosts the measured amplitude by reducing the amount of cancellation between bright and dark spots seen near the limb of the white dwarf.

All of these factors, in addition to the highly uncertain temperatures for DBVs, make the interpretation of a pulsation power versus $T_{\rm eff}$ diagram difficult. Still, we present a current best-effort attempt at producing such a diagram for DBVs so that we can compare with their DAV counterparts. We calculate the total pulsation power (p) for each object by summing the power of each independent mode, $p = \sum_i A_i^2$, again excluding any linear combinations or harmonics. In Figure 8 we present the square root of the total power versus $T_{\rm eff}$ in the top panel and versus the WMP in the bottom panel.

In both panels of Figure 8, the total pulsation power appears to increase from the blue edge to the middle of the instability strip, and then fall back down again at the red edge. This is similar to the DAVs, whose rise in pulsation power from the blue edge has been documented for decades (Robinson 1979, 1980; McGraw 1980; Fontaine et al. 1982; Clemens 1993; Kanaan et al. 2002), while the decrease in power close to the red edge was only observed more recently (Mukadam et al. 2006; Vincent et al. 2020). In combination
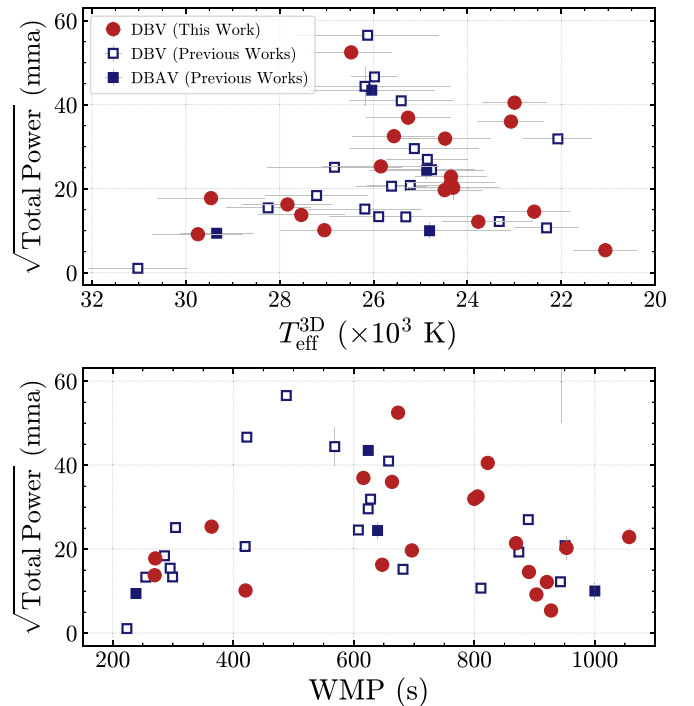

Figure 8. The square root of the maximum power mode vs. $T_{\rm eff}$ (top panel) and vs. the WMP (bottom panel) for each new and previously known DBV. Both panels appear to show a rise in pulsation power from the hot edge toward the middle of the instability strip, followed by a potential decrease toward the cool edge. These trends are again similar to those observed for DAVs (Robinson 1979; McGraw 1980; Clemens 1993; Mukadam et al. 2006; Vincent et al. 2020).

with the WMP versus $T_{\rm eff}$ trends, these qualitative similarities support the idea that DAV and DBV pulsations are being driven by similar mechanisms. Perhaps the main difference seen in the DBV pulsation power, however, is that the peak might happen at lower WMP before falling off. In the DAVs, pulsation power begins to decrease between WMPs of 900 and 1000 s, while for DBVs, it appears to happen somewhat sooner, around 800 s. This small difference, however, might just be a matter of still having too few DBVs to properly sample the power versus WMP diagram.

6. Conclusions

We obtained time-series photometry for 55 DB and DBA white dwarfs located in and near the DB instability strip based on atmospheric parameters determined from SDSS spectra. Of these, we found 19 DBs to pulsate, and placed limits on the variability, often lower than 0.5%, for the remaining 36 objects. Compared to the 28 previously known DBVs, the new DBVs presented here do not significantly extend the DB instability strip in either the hot or cool directions, but improve constraints on the empirical locations of the red (cool) and blue (hot) edges, especially given how uncertain the temperatures for these objects typically are.

After applying the 3D convection corrections determined by Cukanovaite et al. (2021) to spectroscopic $T_{\rm eff}$ and $\log(g)$ from the literature, we find that the most recent theoretical calculations describing the blue- and red-edge locations (Van Grootel et al. 2017) agree well with the empirical DB instability strip, although the observed blue and red edges both appear hotter than the respective theoretical edges. Even so, we caution that we have not used a homogeneous spectroscopic sample, and the differences in

atmospheric models, fitting procedures, and observational data quality between objects can influence the location of the instability strip. In the second paper of this series, we plan to present a homogeneous spectroscopic study of numerous DBVs and NOVs using observations from the Hobby Eberly Telescope at McDonald Observatory.

We found several NOVs within the theoretical instability strip, which can be accounted for with a variety of explanations. Given their large temperature uncertainties, some NOVs may in fact lie outside the instability strip. For others, perhaps the pulsations were undergoing destructive beating during our observations, suppressing the observed pulsation amplitudes below our detection thresholds. Last, some DBVs might just have low-amplitude pulsations, which is especially common among blue-edge pulsators like PG 0112+104. More extensive observations would be required in most cases to rule out pulsations more definitively before assessing the purity of the DB instability strip.

With the larger number of DBVs now available, we presented the first analysis of the ensemble properties of DBVs, investigating how the weighted mean period and total pulsation power change as a function of effective temperature. We find both to exhibit qualitatively similar trends when compared with the DAVs (Clemens 1993; Mukadam et al. 2006), with the weighted mean period increasing gradually with decreasing $T_{\rm eff}$, and the pulsation power initially increasing toward the middle of the instability strip before potentially decreasing toward the cool edge. The similarities in pulsation properties between DAVs and DBVs support the idea that they have a similar driving mechanism.

To further improve constraints on the observed blue and red edges, increasing the number of DBVs is still important, as is performing homogeneous spectroscopic or photometric analyses of as many DBVs and NOVs as possible for $T_{\rm eff}$, $\log(g)$, and [H/He] determinations. After our search, only 40 relatively bright DBs with $g < 19$ mag and $T_{\rm eff}$ between 22,000 and 29,000 K remain in the KK15 catalog that have not yet been assessed for variability. Future spectroscopic surveys covering a much larger area of the sky will be vital for future DBV searches as they will increase the number of spectroscopically confirmed DBs near to and within the instability strip. For example, the SDSS-V Milky Way Mapper plans to obtain hundreds of thousands of optical spectra of white dwarfs as part of its White Dwarf Chronicle survey (Kollmeier et al. 2017), an order-of-magnitude increase in the number of spectroscopically observed white dwarfs. Using variability metrics based on Zwicky Transient Facility and Gaia photometry (e.g., Guidry et al. 2021) may also provide a promising method to efficiently identify some high-amplitude DBVs without prior spectral classifications.

Appendix
Additional Tables

Table 4 provides the atmospheric parameters and some pulsation properties for the new DBVs presented in this work. Table 5 provides the atmospheric properties and variability limits for the new NOVs presented in this work.

Table 5
Atmospheric Parameters and Variability Limits for New NOVs

Name (SDSS J)	Type	P-M-F	g (mag)	$T_{\rm eff}$ (K)	$\log(g)$ (cgs)	[H/He]	$T_{\rm eff}^{\rm 3D}$ (K)	$\log(g)^{\rm 3D}$ (cgs)	NOV[a] (mma)	Runs[a]
002458.42+245834.2	DB	6279-56243-16	17.3	20690[660]	8.07[0.12]	⋯	22130	8.01	2.3	3
014945.65+223016.4	DB	5112-55895-304	19.3	31490[1120]	7.67[0.14]	⋯	31480	7.68	7.1	3
020409.84+212948.5	DBA	5113-55924-232	18.1	20980[660]	8.25[0.12]	−2.99[0.13]	22260	8.23	3.1	2
023402.50+243352.2	DBA	2399-53764-105	19.0	29760[1070]	7.86[0.13]	−2.76[0.08]	29740	7.87	6.1	2
065146.31+271927.3	DB	2694-54199-23	18.2	35800[1190]	7.96[0.13]	⋯	35800	7.96	4.1	2
074925.14+195040.0	DB	4485-55836-185	17.9	19720[620]	7.97[0.12]	⋯	20920	7.90	3.5	2
075452.85+194907.0	DB	4482-55617-368	18.3	21300[710]	7.90[0.12]	⋯	22850	7.86	3.3	2
075523.86+172825.1[b]	DB	2729-54419-106	17.9	27180[870]	7.77[0.12]	⋯	27160	7.77	4.0	2
080349.15+085532.6	DB	2419-54139-98	18.0	21860[760]	7.98[0.13]	⋯	23520	7.95	4.3	2
081656.17+204946.0[b]	DB	1925-53327-573	17.0	27460[870]	7.89[0.12]	⋯	27450	7.89	2.1	3
082316.32+233317.8	DBA	4468-55894-114	17.6	19860[630]	8.08[0.12]	−4.13[0.22]	20930	8.05	3.1	2
084350.85+361419.5	DB	4609-56251-422	17.0	20430[660]	8.03[0.12]	⋯	21810	7.96	1.9	2
084614.89+193515.3	DBA	2280-53680-248	18.1	20560[670]	8.25[0.13]	−3.22[0.24]	21730	8.23	5.4	1
084953.09+105621.2	DB	2671-54141-476	17.9	30530[970]	8.04[0.12]	⋯	30510	8.05	3.3	2
092106.44+140736.7	DBA	5305-55984-134	18.0	22360[730]	8.51[0.12]	−3.39[0.25]	24000	8.49	2.7	3
092355.26+085717.3	DBA	1302-52763-489	16.4	20500[650]	7.96[0.12]	−4.16[0.15]	21750	7.94	1.4	2
105423.94+211057.4	DB	6427-56328-162	17.3	22010[740]	7.95[0.12]	⋯	23660	7.92	1.8	2
112752.92+553522.0	DBA	7093-56657-80	17.1	19640[620]	8.19[0.12]	−4.17[0.13]	20620	8.15	2.3	2
113247.25+283519.0[b]	DB	2217-53794-50	18.7	25260[990]	7.97[0.13]	⋯	25680	7.96	4.1	2
131646.02+414639.0	DB	1460-53118-535	17.2	21840[720]	7.95[0.12]	⋯	23490	7.92	2.2	2
140028.43+475644.1	DB	6750-56367-648	17.1	30830[980]	7.92[0.12]	⋯	30810	7.92	2.3	2
142405.54+181807.3	DB	2760-54506-374	18.8	30010[1100]	8.00[0.12]	⋯	29990	8.00	4.4	2
144814.33+150449.7	DB	2750-54242-334	15.7	20330[640]	7.93[0.12]	⋯	21690	7.87	1.9	2
145755.43+015442.9	DB	4015-55624-316	18.1	19600[620]	8.00[0.12]	⋯	20760	7.93	3.6	2
151729.46+433028.6	DB	1678-53433-372	18.3	28930[970]	8.00[0.12]	⋯	28920	8.00	11.4	1
153454.99+224918.6	DB	2162-54207-528	17.6	20800[680]	8.01[0.13]	⋯	22270	7.95	3.4	2
154201.50+502532.1	DB	796-52401-180	16.8	31030[990]	7.64[0.12]	⋯	31010	7.65	1.4	2
155921.08+190407.8	DBA	3930-55332-259	16.4	20680[650]	7.99[0.12]	−3.80[0.16]	21960	7.97	2.0	3
174025.00+245705.5	DBA	2183-53536-303	17.5	20440[650]	8.33[0.13]	−3.31[0.19]	21560	8.30	2.4	2
183252.20+421526.1	DB	2819-54617-322	17.8	21400[710]	7.92[0.12]	⋯	22970	7.87	2.2	2
214441.71+010029.8	DB	4196-55478-714	18.3	20080[650]	7.96[0.12]	⋯	21380	7.89	4.9	2
220250.26+213120.2	DB	5948-56107-107	16.9	20290[640]	7.99[0.12]	⋯	21640	7.92	2.2	2
222833.82+141036.9	DB	737-52518-602	18.8	31720[1220]	7.76[0.15]	⋯	31710	7.76	3.6	2
232108.40+010433.5	DB	382-51816-614	18.1	21040[870]	8.14[0.14]	⋯	22570	8.08	4.1	2
232711.11+515344.7	DB	1662-52970-96	17.3	30510[990]	7.84[0.13]	⋯	30490	7.84	1.3	3
234848.77+381754.6[b]	DB	1882-53262-136	17.5	23920[880]	8.06[0.13]	⋯	25400	8.05	2.1	2

Notes. SDSS J065146.31+271927.3 falls outside the 3D correction grids of Cukanovaite et al. (2021), so the 3D-corrected values for this object are the same as the 1D values. The spectral types displayed are based solely on the detection (DBA) or nondetection (DB) of trace H in the SDSS spectra analyzed by KK15 and Kepler et al. (2019), and may differ from previous spectral classifications.
[a] NOV represents the not-observed-to-vary limit from our McDonald runs, while the number of runs indicates for how many individual nights an object was observed not to vary.
[b] NOVs more than 1σ inside the theoretical instability strip and with variability limits <5 mma, as shown in Figure 4.

ORCID iDs

Zachary P. Vanderbosch ● https://orcid.org/0000-0002-0853-3464
J. J. Hermes ● https://orcid.org/0000-0001-5941-2286
Don E. Winget ● https://orcid.org/0000-0003-0181-2521
Michael H. Montgomery ● https://orcid.org/0000-0002-6748-1748
Keaton J. Bell ● https://orcid.org/0000-0002-0656-032X
S. O. Kepler ● https://orcid.org/0000-0002-7470-5703

References

Astropy Collaboration, Price-Whelan, A. M., Sipőcz, B. M., et al. 2018, AJ, 156, 123
Bailer-Jones, C. A. L., Rybizki, J., Fouesneau, M., Demleitner, M., & Andrae, R. 2021, AJ, 161, 147
Battich, T., Córsico, A. H., Althaus, L. G., & Miller Bertolami, M. M. 2016, JCAP, 2016, 062
Bauer, E. B., & Bildsten, L. 2019, ApJ, 872, 96
Beauchamp, A., Wesemael, F., Bergeron, P., et al. 1999, ApJ, 516, 887
Bédard, A., Bergeron, P., Brassard, P., & Fontaine, G. 2020, ApJ, 901, 93
Bell, K. J., Córsico, A. H., Bischoff-Kim, A., et al. 2019, A&A, 632, A42
Bell, K. J., Gianninas, A., Hermes, J. J., et al. 2017b, ApJ, 835, 180
Bell, K. J., Hermes, J. J., Vanderbosch, Z., et al. 2017a, ApJ, 851, 24
Bell, K. J., Pelisoli, I., Kepler, S. O., et al. 2018, A&A, 617, A6
Bergeron, P., Dufour, P., Fontaine, G., et al. 2019, ApJ, 876, 67
Bergeron, P., Ruiz, M. T., & Leggett, S. K. 1997, ApJS, 108, 339
Bergeron, P., Wesemael, F., Dufour, P., et al. 2011, ApJ, 737, 28
Bischoff-Kim, A., Østensen, R. H., Hermes, J. J., & Provencal, J. L. 2014, ApJ, 794, 39
Bischoff-Kim, A., Provencal, J. L., Bradley, P. A., et al. 2019, ApJ, 871, 13
Blanton, M. R., Bershady, M. A., Abolfathi, B., et al. 2017, AJ, 154, 28
Bognár, Z., Paparó, M., Córsico, A. H., Kepler, S. O., & Győrffy, Á. 2014, A&A, 570, A116
Böhm, K. H., & Cassinelli, J. 1971, A&A, 12, 21
Böhm-Vitense, E. 1958, ZAp, 46, 108
Breger, M., Stich, J., Garrido, R., et al. 1993, A&A, 271, 482
Brickhill, A. J. 1991, MNRAS, 251, 673

Castanheira, B. G., Kepler, S. O., Kleinman, S. J., Nitta, A., & Fraga, L. 2010, MNRAS, 405, 2561
Charpinet, S., Brassard, P., Giammichele, N., & Fontaine, G. 2019, A&A, 628, L2
Clemens, J. C. 1993, BaltA, 2, 407
Clemens, J. C. 1994, PhD thesis, Univ. Texas at Austin
Córsico, A. H., Althaus, L. G., Miller Bertolami, M. M., & García-Berro, E. 2009, JPhCS, 172, 012075
Córsico, A. H., Althaus, L. G., Miller Bertolami, M. M., & Kepler, S. O. 2019, A&ARv, 27, 7
Cukanovaite, E., Tremblay, P.-E., Bergeron, P., et al. 2021, MNRAS, 501, 5274
Cukanovaite, E., Tremblay, P. E., Freytag, B., Ludwig, H. G., & Bergeron, P. 2018, MNRAS, 481, 1522
Dalessio, J., Sullivan, D. J., Provencal, J. L., et al. 2013, ApJ, 765, 5
Duan, R. M., Zong, W., Fu, J. N., et al. 2021, ApJ, 922, 2
Dufour, P., Desharnais, S., Wesemael, F., et al. 2010b, ApJ, 718, 647
Dufour, P., Kilic, M., Fontaine, G., et al. 2010a, ApJ, 719, 803
Eisenstein, D. J., Liebert, J., Harris, H. C., et al. 2006b, ApJS, 167, 40
Eisenstein, D. J., Liebert, J., Koester, D., et al. 2006a, AJ, 132, 676
Eisenstein, D. J., Weinberg, D. H., Agol, E., et al. 2011, AJ, 142, 72
Farihi, J., Gänsicke, B. T., & Koester, D. 2013, Sci, 342, 218
Farihi, J., Koester, D., Zuckerman, B., et al. 2016, MNRAS, 463, 3186
Fontaine, G., & Brassard, P. 2008, PASP, 120, 1043
Fontaine, G., McGraw, J. T., Dearborn, D. S. P., Gustafson, J., & Lacombe, P. 1982, ApJ, 258, 651
Fuchs, J. T. 2017, PhD thesis, The University of North Carolina at Chapel Hill
Genest-Beaulieu, C., & Bergeron, P. 2019a, ApJ, 871, 169
Genest-Beaulieu, C., & Bergeron, P. 2019b, ApJ, 882, 106
Gentile Fusillo, N. P., Tremblay, P. E., Cukanovaite, E., et al. 2021, MNRAS, 508, 3877
Gentile Fusillo, N. P., Tremblay, P.-E., Gänsicke, B. T., et al. 2019, MNRAS, 482, 4570
Giammichele, N., Charpinet, S., Fontaine, G., et al. 2018, Natur, 554, 73
Goldreich, P., & Wu, Y. 1999, ApJ, 511, 904
Guidry, J. A., Vanderbosch, Z. P., Hermes, J. J., et al. 2021, ApJ, 912, 125
Handler, G. 2001, MNRAS, 323, L43
Handler, G., Metcalfe, T. S., & Wood, M. A. 2002, MNRAS, 335, 698
Handler, G., O'Donoghue, D., Müller, M., et al. 2003, MNRAS, 340, 1031
Hermes, J. J., Gänsicke, B. T., Kawaler, S. D., et al. 2017b, ApJS, 232, 23
Hermes, J. J., Kawaler, S. D., Bischoff-Kim, A., et al. 2017a, ApJ, 835, 277
Hoskin, M. J., Toloza, O., Gänsicke, B. T., et al. 2020, MNRAS, 499, 171
Kanaan, A., Kepler, S. O., & Winget, D. E. 2002, A&A, 389, 896
Kepler, S. O., Pelisoli, I., Koester, D., et al. 2015, MNRAS, 446, 4078
Kepler, S. O., Pelisoli, I., Koester, D., et al. 2016, MNRAS, 455, 3413
Kepler, S. O., Pelisoli, I., Koester, D., et al. 2019, MNRAS, 486, 2169
Kepler, S. O., Winget, D. E., Vanderbosch, Z. P., et al. 2021, ApJ, 906, 7
Kilkenny, D., O'Donoghue, D., Crause, L. A., Hambly, N., & MacGillivray, H. 2009, MNRAS, 397, 453
Kleinman, S. J., Harris, H. C., Eisenstein, D. J., et al. 2004, ApJ, 607, 426
Kleinman, S. J., Kepler, S. O., Koester, D., et al. 2013, ApJS, 204, 5
Koester, D., & Kepler, S. O. 2015, A&A, 583, A86
Koester, D., Provencal, J., & Gänsicke, B. T. 2014, A&A, 568, A118
Kollmeier, J. A., Zasowski, G., Rix, H.-W., et al. 2017, arXiv:1711.03234
Kong, X., Luo, A. L., Li, X.-R., et al. 2018, PASP, 130, 084203
Kuschnig, R., Weiss, W. W., Gruber, R., Bely, P. Y., & Jenkner, H. 1997, A&A, 328, 544
Landolt, A. U. 1968, ApJ, 153, 151
Lenz, P., & Breger, M. 2004, in The A-Star Puzzle, IAU Symp. 224, ed. J. Zverko et al. (Cambridge: Cambridge Univ. Press), 786
MacDonald, J., & Vennes, S. 1991, ApJ, 371, 719
McCook, G. P., & Sion, E. M. 1999, ApJS, 121, 1
McGraw, J. T. 1980, SSRv, 27, 601
Melis, C., Farihi, J., Dufour, P., et al. 2011, ApJ, 732, 90

Metcalfe, T. S., Montgomery, M. H., & Kanaan, A. 2005, in 14th European Workshop on White Dwarfs, ASP Conf. Ser. 334, ed. D. Koester & S. Moehler (San Francisco, CA: ASP)
Montgomery, M. H. 2005, ApJ, 633, 1142
Montgomery, M. H., Hermes, J. J., Winget, D. E., Dunlap, B. H., & Bell, K. J. 2020, ApJ, 890, 11
Montgomery, M. H., & Odonoghue, D. 1999, DSSN, 13, 28
Mukadam, A. S., Montgomery, M. H., Winget, D. E., Kepler, S. O., & Clemens, J. C. 2006, ApJ, 640, 956
Mukadam, A. S., Nather, R. E., et al. 2004, ApJ, 607, 982
Mullally, F., Winget, D. E., Degennaro, S., et al. 2008, ApJ, 676, 573
Nather, R. E., Robinson, E. L., & Stover, R. J. 1981, ApJ, 244, 269
Nitta, A., Kleinman, S. J., Krzesinski, J., et al. 2009, ApJ, 690, 560
Østensen, R. H., Bloemen, S., Vučković, M., et al. 2011, ApJL, 736, L39
Provencal, J. L., Montgomery, M. H., Kanaan, A., et al. 2009, ApJ, 693, 564
Provencal, J. L., Shipman, H. L., Riddle, R. L., & Vuckovic, M. 2003, in NATO Advanced Study Institute (ASI) Series B, White Dwarfs, ed. D. de Martino, Vol. 105 (Princeton, NJ: NATO), 235
Redaelli, M., Kepler, S. O., Costa, J. E. S., et al. 2011, MNRAS, 415, 1220
Robinson, E. L. 1979, in IAU Colloq. 53: White Dwarfs and Variable Degenerate Stars, ed. H. M. van Horn, V. Weidemann, & M. P. Savedoff (Dordrecht: Kluwer), 343
Robinson, E. L. 1980, The pulsating white dwarfs (Washington, DC: NASA), 423
Robinson, E. L., Kepler, S. O., & Nather, R. E. 1982, ApJ, 259, 219
Rolland, B., Bergeron, P., & Fontaine, G. 2018, ApJ, 857, 56
Rowan, D. M., Tucker, M. A., Shappee, B. J., & Hermes, J. J. 2019, MNRAS, 486, 4574
Shipman, H. L., Provencal, J., Riddle, R., & Vuckovic, M. 2002, AAS Meeting Abstracts, 200, 72.06
Sullivan, D. J. 2017, in ASP Conf. Ser. 509, 20th European White Dwarf Workshop, ed. P. E. Tremblay, B. Gaensicke, & T. Marsh (San Francisco, CA: ASP), 315
Sullivan, D. J., Metcalfe, T. S., O'Donoghue, D., et al. 2008, MNRAS, 387, 137
Tassoul, M., Fontaine, G., & Winget, D. E. 1990, ApJS, 72, 335
Thompson, S., & Mullally, F. 2013, Wqed: Lightcurve Analysis Suite, Astrophysics Source Code Library, ascl:1304.004
Timmes, F. X., Townsend, R. H. D., Bauer, E. B., et al. 2018, ApJL, 867, L30
Van Grootel, V., Fontaine, G., Brassard, P., & Dupret, M. A. 2017, in ASP Conf. Ser. 509, The Theoretical Instability Strip of V777 Her White Dwarfs, ed. P. E. Tremblay, B. Gaensicke, & T. Marsh (San Francisco, CA: ASP), 321
Vincent, O., Bergeron, P., & Lafrenière, D. 2020, AJ, 160, 252
Voss, B., Koester, D., Napiwotzki, R., Christlieb, N., & Reimers, D. 2007, A&A, 470, 1079
Winget, D. E., Cochran, W. D., Endl, M., et al. 2003, in ASP Conf. Ser. 294, Scientific Frontiers in Research on Extrasolar Planets, ed. D. Deming & S. Seager (San Francisco, CA: ASP), 59
Winget, D. E., & Fontaine, G. 1982, in Pulsations in Classical and Cataclysmic Variable Stars (Boulder, CO: Joint Institute for Laboratory Astrophysics), 46
Winget, D. E., Nather, R. E., & Hill, J. A. 1987, ApJ, 316, 305
Winget, D. E., Robinson, E. L., Nather, R. D., & Fontaine, G. 1982, ApJL, 262, L11
Winget, D. E., Sullivan, D. J., Metcalfe, T. S., Kawaler, S. D., & Montgomery, M. H. 2004, ApJL, 602, L109
Wu, Y. 2001, MNRAS, 323, 248
Wu, Y., & Goldreich, P. 1999, ApJ, 519, 783
Xu, S., Dufour, P., Klein, B., et al. 2019, AJ, 158, 242
York, D. G., Adelman, J. A., John, E. J., et al. 2000, AJ, 120, 1579
Zuckerman, B., Koester, D., Melis, C., Hansen, B. M., & Jura, M. 2007, ApJ, 671, 872